J. Mech. Phys. Solids 175 (2023) 105293

Contents lists available at ScienceDirect

Journal of the Mechanics and Physics of Solids

journal homepage: www.elsevier.com/locate/jmps

A framework to simulate the crack initiation and propagation in very-high-cycle fatigue of an additively manufactured AlSi10Mg alloy

Jingyu Sun [a,*], Guian Qian [a,*], Jianghua Li [a], Ruiyang Li [b], Zhimo Jian [a], Youshi Hong [a], Filippo Berto [c]

[a] State Key Laboratory of Nonlinear Mechanics (LNM), Institute of Mechanics, Chinese Academy of Sciences, Beijing 100190, China
[b] College of Mechanical Engineering, Guangxi University, Nanning 530004, China
[c] Department of Mechanical and Industrial Engineering, Norwegian University of Science and Technology (NTNU), Richard Birkelands vei 2b, Trondheim 7491, Norway

ARTICLE INFO

Keywords:
Crystal plasticity
Cohesive zone model
Very-high-cycle fatigue
Microstructure-sensitive fatigue
Short crack growth

ABSTRACT

Currently, no systematic approach exists to simulate the crack initiation and propagation process in very-high-cycle fatigue including the microstructure sensitivity. A combined crystal plasticity and cohesive zone model based computational framework is developed to simulate the defect-induced short crack growth of an additively manufactured AlSi10Mg alloy. The crystal plasticity formulation is used to model the anisotropic deformation in the grains. The accumulated plastic shear strain obtained by the crystal plasticity is introduced into the cohesive zone model as the crack initiation damage evolution criteria. The total damage is suggested to be divided into static damage, fatigue initiation damage and fatigue propagation damage. The framework can control the crack growth rate and the proportion of crack initiation damage in the total damage. Besides, an acceleration strategy is proposed to accelerate the computational efficiency for the very-high-cycle fatigue (VHCF). It provides an equivalence of loading cycles and the computational efficiency and accuracy are controlled by the acceleration factor. The internal defect induced short crack initiation and propagation of VHCF are investigated experimentally and simulated by the proposed framework. Experimental observations of tortuous crack paths and fine grain regions are reasonably well captured by the simulation.

1. Introduction

Additive manufacturing (AM) has been developing rapidly in the last 30 years, and it has unique advantages in producing components with complex geometries (Liu et al., 2021b). Laser powder bed fusion (LPBF) technology is a layer-by-layer powder-bed AM method and its high cooling rate (10^3–10^5 K/s) during the construction process induces finer grain size of the LPBF metal than the cast one, which enhances the tensile properties (Li et al., 2015a). However, limited by the current technology, the internal defects cannot be eliminated absolutely in the LPBF metal, such as lack of fusions (LOF), voids, and inclusions (Bellini et al., 2021). The fatigue properties of the LPBF metal are reduced by the internal defects (Zhang et al., 2022; Li et al., 2022b). For very-high-cycle fatigue (VHCF), the crack initiation is highly dependent on the defects and microstructure of the material (Wang et al., 1999). Thus,

* Corresponding authors.
E-mail addresses: sunjingyu@imech.ac.cn (J. Sun), qianguian@imech.ac.cn (G. Qian).

https://doi.org/10.1016/j.jmps.2023.105293
Received 4 July 2022; Received in revised form 22 March 2023; Accepted 30 March 2023
Available online 5 April 2023

Nomenclature

δ_{ij}	Kronecker delta
η	Interpolation parameter
ε_{ij}	Strain tensor
$\Omega_{ij}^{(\alpha)}$	Slip spin tensor
κ	Slip strength
ψ	Free energy per unit surface of the interface
ψ^0	No damage free energy
$\rho^{(\alpha)}$	Dislocation hardening parameter of CPFEM
σ_{ij}	Cauchy stress
$\tau^{(\alpha)}$	Resolved shear stress on the α-th slip system
θ_i	Separations in the local coordinates
θ_{sh}	Norm of the separations in shear mode
θ_{th}	Threshold of separation
$\tilde{\theta}^0$	Equivalent onset displacement jump
$\tilde{\theta}^{\mathrm{f}}$	Equivalent failure separation
η	Semi-empirical coefficient of mixed-mode CZM
$\alpha^{(\alpha)}$	Back stress on the α-th slip system
$\dot{\gamma}^{(\alpha)}$	Plastic slip rate of the α-th slip system
$\dot{\gamma}_0$	Reference strain rate
A	Crack area
A_{CZ}	Cohesive zone area
A_{d}	Damaged area
A_{e}	Element area
b	Isotropic hardening parameter of CPFEM
B	Fatigue propagation parameter of CZM
$B_{ij}^{(\alpha)}$	Coefficient matrix
C	Fatigue propagation parameter of CZM
C_{acc}	Acceleration coefficient
C_{ij}^0	Elastic stiffness tensor of CZM
$\mathbb{C}_{ijkl}$	Elastic stiffness tensor of CPFEM
c_1, c_2	Kinematic hardening parameters of CPFEM
d	Total damage
d_{init}	Fatigue initiation damage
d_{prop}	Fatigue propagation damage
d_{static}	Quasi-static damage
D_{ij}	Symmetric part of velocity gradient L_{ij}
E_{K}	Penalty stiffness
$f, f_{\mathrm{exp}}, f_{\mathrm{ref}}, f_{\mathrm{sim}}$	Load frequencies
f_{acc}	Acceleration function
$F_{ij}, F_{ij}^{\mathrm{e}}, F_{ij}^{\mathrm{p}}$	Deformation gradient tensor
G	Energy release rate
G_{c}	Critical energy release rate
G_{sh}	Shear energy release rate
G_{th}	Fatigue threshold of the energy release rate
ΔG	Cyclic variation of the energy release rate
$h_{\alpha\beta}$	Hardening matrix
H_{V}	Vickers hardness

it is necessary to investigate the mechanism of how the crack initiation and propagation process is affected by defects in the VHCF regime.

The mechanism of crack initiation and early growth for VHCF is significantly different from that for low-cycle fatigue (LCF) and high-cycle fatigue (HCF), especially for negative stress ratios. For example, the crack initiation characteristic region of VHCF

K	Stress intensity factor
ΔK	Stress intensity factor range
ΔK_{th}	Threshold of stress intensity factor range
$L_{ij}, L_{ij}^{\mathrm{p}}$	Velocity gradient tensor
m	Fatigue propagation parameter of CZM
M	Total number of slip system
n	Rate sensitive factor of CPFEM
$n_i^{(\alpha)}$	Slip normal plane vector of the α-th slip system
N	Number of cycles
p	Accumulated plastic strain
$P_{ij}^{(\alpha)}$	Schmid tensor
Q	Isotropic hardening parameter of CPFEM
$r^{(\alpha)}$	Resistance stress on the α-th slip system
R	Stress ratio
R_θ	Damage consistency parameter
s	Time variable
$s_i^{(\alpha)}$	Slip direction vector of the α-th slip system
t	Time variable
t_b	Thickness
T_i	Tractions in the local coordinates
T^0, T_1^0, T_2^0, T_3^0	Interfacial strength
W_{ij}	Antisymmetric part of velocity gradient L_{ij}
x	Variable of function or x coordinate
X	Internal variable of CPFEM

generally contains a rough region of fine-granular-area (FGA) around the crack origin, i.e., fish-eye (FiE) (Hong et al., 2016). Several mechanisms of crack initiation and early growth for VHCF have been proposed, including "decohesion of spherical carbide" (Shiozawa et al., 2006), "formation and debonding of fine granular layer" (Sakai et al., 2015) and "number cyclic pressing (NCP) model" (Hong et al., 2016). Among them, the NCP model has been recognized and successfully applied to explain the formation of the fine-grained layer and the trend of decreasing FGA size with increasing stress ratio for different metallic materials (Zhang et al., 2021; Pan and Hong, 2019; Ritz et al., 2018). The results show that the repeated pressing of the crack surface under cyclic loading causes local severe plastic deformation. This leads to the local dislocation pile-up near the crack surface and large crystal misorientation, and finally evolves into large-angle grain boundaries showing the grain refinement characteristics (Zhu et al., 2018; Sun et al., 2022; Li et al., 2022a). Ogawa et al. (2014) and Sander et al. (2014) showed that the fatigue short crack growth under VHCF was a discontinuous process, and the crack growth rate (10^{11}–10^{14} m/cycle) was significantly lower than the interatomic distance. It indicates that the crack does not propagate in every loading cycle, and many experimental results have confirmed this conclusion (Ogawa et al., 2014; Hong et al., 2014). Therefore, the fraction of fatigue life due to crack initiation (Stage I) at FGA is estimated, and the FGA region consumes more than 95% of total fatigue life (Hong et al., 2014; Su et al., 2017).

In FGA, the stress and strain fields near the crack tip are influenced by the microstructure of the material, thus the isotropy assumption is no longer appropriate. VHCF cracks usually initiate at the internal or at the subsurface of the material, so it is difficult to investigate the crack initiation and propagation mechanism by experimental observations. Therefore, a numerical simulation method was introduced to investigate this mechanism. Mughrabi (2009) found that, within the crystal near the defects, irreversible plastic deformation occurs due to the interaction of dislocations. Moreover, the crack nucleation may occur as a result of the accumulation of cyclic plastic deformation. Next, the emerging crack nuclei will develop once it breaks through the first microstructural barrier such as grain or phase boundaries, which ultimately leads to macroscopic fatigue initiation (Bach et al., 2016; Strubbia et al., 2014). In HCF/VHCF regimes, LPBF alloys usually fail near defects, and those defects whose size is close to the grain size would be preferred (Gu et al., 2022). Furthermore, the grain size, shape, orientation, etc. will influence the local plastic deformation caused by stress concentration near defects (Cong et al., 2022; Hu et al., 2019). With the accumulation of plastic strain, the hardening of the crystal itself leads to the redistribution of stress and further localization of plastic deformation. Therefore, the numerical simulation should capture this process accurately.

The crystal plasticity finite element model (CPFEM) simulation is widely used to investigate the fracture damage of metallic materials with considering the effects of microstructure and anisotropy, which was first proposed by Peirce et al. (1982). The crystal plasticity theory developed the plastic flow model, work-hardening model, and internal variable evolution model (e.g. dislocation density), which conform to the plastic deformation mechanism. Since it is based on the grain scale, various mechanical effects could be coupled, such as grain size/orientation, texture, damage, etc. (Roy et al., 2021). With rapid improvements in computational methods and devices, lots of CPFEM simulations have been carried out. There are two types of crystal plasticity constitutive models.

The most popular type is phenomenological constitutive models (Asgharzadeh et al., 2022; Huang et al., 2021; Morgeneyer et al., 2021; Shang et al., 2021) while the other is microstructure-based constitutive models (Asgharzadeh et al., 2022; Cheng et al., 2021; Li et al., 2016; Min et al., 2020). Generally, the microstructure-based constitutive models are built from a microscopic mechanism, with quantifiable microstructural parameters (usually using dislocation density) as state variables. Results calculated by microstructure-based constitutive models are more accurate than phenomenological constitutive models but the computational cost is higher as well. The development of crystal plasticity theory has been well summarized by Roters et al. (2010).

Recently, with the superior flexible CPFEM framework, some interesting investigations were reported on the fatigue and fracture field. Li et al. (2021) quantitatively analyzed the effect of orientation difference on the fatigue life of nickel-based single crystal alloys, and showed that the damage accumulation at the time of crack initiation caused by slip within the crystal. Zhang et al. (2022) investigated the VHCF behavior of an additively manufactured Al alloy with a 2D Voronoi RVE model and investigated how defects affect the VHCF life. They found that as fatigue life increased, cracks tended to initiate from the interior rather than the surface, which is consistent with the experimental results (Jian et al., 2021; Li et al., 2022b). Indeck et al. (2021) effectively predicted slip activity for any arbitrary grain orientation by integrating the machine learning technique with CPFEM. In addition, Briffod et al. (2018) evaluated the effects of polycrystal grain morphology and texture on fatigue crack initiation, and the shear rate on each slip system was modeled with a phenomenological constitutive law.

To better simulate the process of crack initiation and propagation, the cohesive zone model (CZM) was introduced to describe the interface contact and friction behavior during cyclic loading. In the simulation of microcrack initiation and propagation at grain scale, the form of CZM is in accord with the intergranular and intragranular mechanical laws as well. The concept of CZM was originally introduced by Barenblatt (1962) and Dugdale (1960). Later, CZM became popular with the effort of Turon et al. (2007) and the subsequent implementation in commercial finite element codes. Nowadays, most CZM mechanical behaviors were described with traction-separation law. The maximum traction force represents the cohesive strength, and the area under the traction separation curve represents fracture energy. The damage process is described by decreasing cohesive traction with increasing separation. Once the separation reaches a critical value, failure occurs.

For monotonic loading, the traction-separation law is independent of the loading path. The relationship between traction and separation is unique and reversible before damage occurs (Yuan and Li, 2018; Molter et al., 2021). For cyclic loading, although the load is below critical traction, the damage will occur if the stress intensity factor is higher than the material threshold (Roe and Siegmund, 2003; Liang et al., 2021). Therefore, additional characteristic parameters should be introduced to evaluate this accumulative damage. Li et al. (2015b)) assumed the total damage as the sum of monotonic damage and cyclic damage. In finite element methods, there are two ways to apply cyclic loading. One is mainly employed in the low cycle of fatigue (LCF) simulations, which completely consider the cycle-by-cycle loading path, and means a higher computation cost. The other one is the cycle-jump strategy proposed by Paepegem et al. (2001). They consider that each skipped cycle causes the same cyclic damage as the last calculated cycle. The accuracy is controlled by controlling the accumulated cyclic damage of skipped cycles during each calculation. To perform a layered HCF simulation, Turon et al. (2010) proposed a damage area ($\mathrm{d}A/\mathrm{d}N$) model using the cycle-jump strategy. Computational results are consistent well with experiments under constant amplitude loading. Nguyen et al. (2019) employed different cyclic damage thresholds of one jump to confirm the cycle jump strategy, and found that the results were very consistent with the original experimental curve.

In recent years, the CPFEM and CZM coupling method (CPFEM-CZM) has been used to study the fracture behavior of metals in grain scale. (Roy et al., 2021) extended their previous work (Roy and Zhou, 2020), by considering the effect of grain orientation on polycrystalline metals. They also discussed whether 2D models can explain 3D behavior by comparing the results obtained from 2D models and 2.5D models. Liu et al. (2021a) investigated the mechanism of transgranular and intergranular fracture of a grain-gradient aluminum by coupled CPFEM with a bilinear CZM, where parameters of the CZM were determined by molecular dynamic simulations. These researches above correlated fracture toughness with material microstructure well, nevertheless, the case of cyclic loading was not considered.

In the field of fatigue and fracture, the CPFEM-CZM method was rarely employed. To analyze the effect of grain orientation on second-stage fatigue crack propagation within a single crystal, Zhao et al. (2021) developed a method that combined CPFEM, XFEM, and CZM. Based on the critical surface method, Ghodrati et al. (2019) introduced a multi-axial fatigue damage factor in CPFEM-CZM to study the rolling contact fatigue of steel. Bergsmo and Dunne (2020) investigated the competition mechanism between particle fracture and particle/matrix decohesion on slip-driven fatigue crack nucleation by energy storage density, which was achieved by integrating the dislocation-based crystal plasticity model with bilinear CZM. In the above-mentioned studies, CZM elements and structural elements share nodes at the interface to solve for the displacement field. The CZM elements themselves cannot obtain the internal variables of nearby elements, which makes it difficult to describe the process of crack nucleation and initiation.

In this study, the crack initiation and propagation mechanism of LPBF aluminum alloy under VHCF is investigated experimentally and computationally. A coupled CPFEM-CZM method is proposed to simulate the crack initiation and propagation behavior of small cracks near the defects under VHCF loading conditions. For the first time, the internal variables of crystal slip computed in the solid elements are introduced into the cohesive zone elements as damage parameters during the crack initiation process, which provides real-time communication between the CZM element and the neighboring solid elements. Meanwhile, for the constant amplitude loading case, an acceleration algorithm is used to achieve the fatigue crack initiation and propagation process simulation under the VHCF loadings, and the model parameters will be corrected by comparing with the experiments.

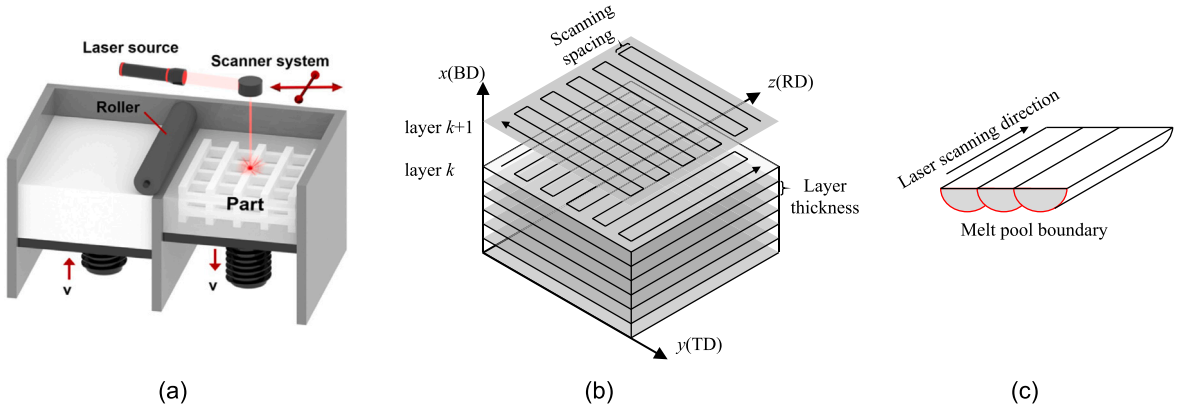

Fig. 1. (a) Schematic of the LPBF process (Liu et al., 2021b). (b) Layer-by-layer scanning. (c) Location of the melt pool boundary.

Table 1
Chemical composition of the AlSi10Mg alloy powder (wt.%).

Al	Si	Mg	Fe	Ti	Cu	Cr	Mn	Ni
Bal.	9.75	0.22	0.092	0.011	<0.01	<0.01	<0.01	<0.01

Table 2
LPBF manufacturing parameters of the investigated AlSi10Mg specimen.

Laser power, W	Scanning speed, mm/s	Scanning spacing, mm	Preheating temperature, °C	Layer thickness, mm	Laser profile
370	1300	0.19	35	0.05	Gaussian

2. Experiment

2.1. Material

2.1.1. Physical properties and manufacturing parameters

The main chemical composition of the AlSi10Mg powder is listed in Table 1. The laser powder bed fusion process is shown in Fig. 1(a). A laser beam is reflected and controlled by a scanner system to melt the metal powder. LPBF AlSi10Mg round bars with a diameter of 16 mm and a length of 52 mm were manufactured with the EOS M290 machine. The building direction is from bottom to up with the scanning spacing of 0.19 mm and the layer thickness of 0.05 mm, as shown in Fig. 1(b). The detailed LPBF parameters were laser power of 370 W, scanning speed of 1300 mm/s, and preheating temperature of 35 °C, as listed in Table 2. The coordinate system BD, TD, and RD in Fig. 1(b) refer to the build direction, tangential direction, and radial direction, respectively. Fig. 1(c) shows the location of melt pool boundary, which is the specific microstructure of the LPBF metals. No heat treatment was carried out for the LPBF AlSi10Mg round bars.

2.1.2. Initial microstructure of the LPBF AlSi10Mg

In this study, the initial microstructure of the LPBF AlSi10Mg alloy was observed by using electron back scatter diffraction (EBSD) and synchrotron radiation X-ray microimaging (SR-μCT). The initial grain features of the LPBF AlSi10Mg alloy were characterized by EBSD using an FEI Nova 400 scanning electron microscope. Fig. 2(a) demonstrates that the investigated LPBF AlSi10Mg alloy contains a large number of columnar grains along the building direction, and the observations reveal that the columnar grains have a maximum length of about 100 μm and a maximum width of about 15 μm. Columnar crystals were not observed in the plane perpendicular to the building direction (Fig. 2(b)), and the grain size was finer at the melt pool boundary than inside the melt pool. Fig. 2(c) and (d) show the {001} pole figure in the BD-TD plane and TD-RD plane, respectively. It is found that the LPBF AlSi10Mg alloy exhibits a {001} texture, characterized by the distribution of the dominant basal pole densities near the BD and RD.

The BL13W1 SR-μCT at the Shanghai Synchrotron Radiation Facility was used to image the material in three dimensions to obtain the distribution of initial defects. A Hamamatsu Flash 4.0 sCMOS detector with a monochromatic X-ray beam of 28 keV was used. The distance between the sample and detector was 18 cm and the pixel size was 3.25 μm. The distribution of initial defects in the LPBF AlSi10Mg alloy is presented in Fig. 3(a). The sphericity and equivalent diameter of the initial defects are shown in Fig. 3(b). The sphericity of 1 represents a perfect sphere and the equivalent diameter is defined as the diameter of an equivalent sphere by volume. In Fig. 3(b), the corresponding number fraction of defects with different equivalent diameters presents that most defects are ellipsoid shapes with an equivalent diameter of less than 40 μm. The smaller spherical defects are usually air holes created during the LPBF process, while the larger irregular defects are mostly lack of fusion defects, which are usually located at the melt pool boundaries.

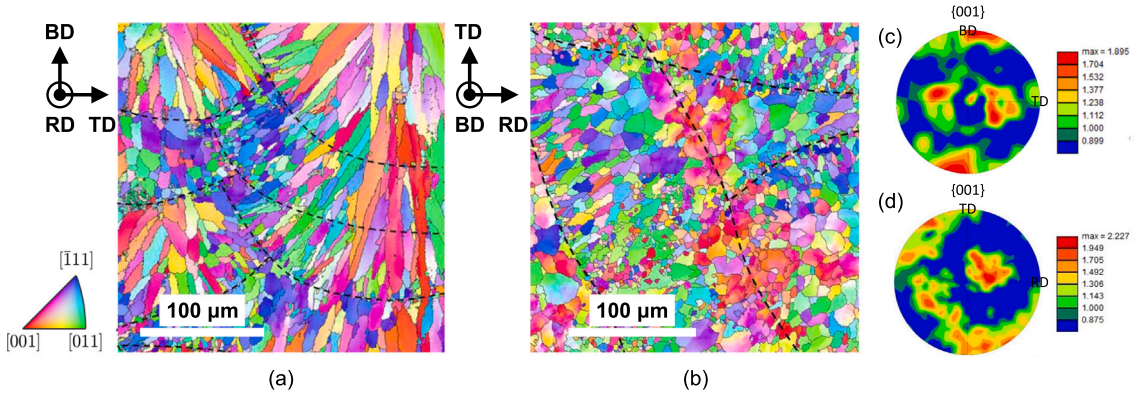

Fig. 2. EBSD inverse pole figure (IPF) maps of the LPBF AlSi10Mg alloy to the plane (a) parallel to the build direction and (b) perpendicular to the build direction. And the {001} pole figure of (c) BD-TD plane and (d) TD-RD plane.

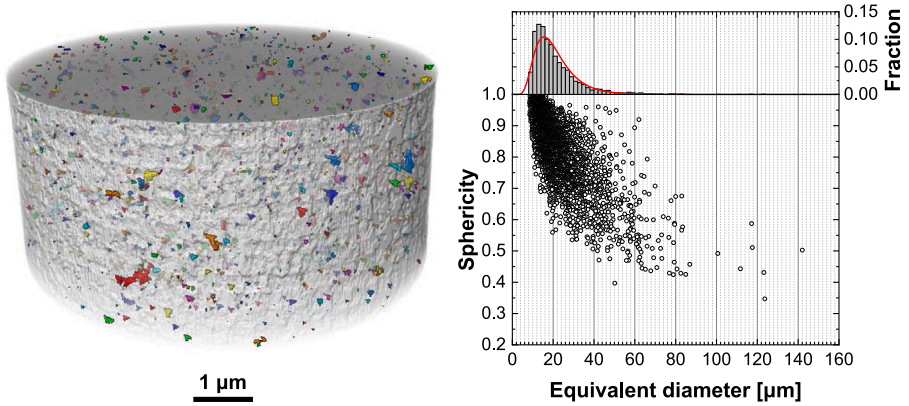

Fig. 3. (a) Defects measured by SR-μCT technology. (b) Statistical analysis of the defects.

2.2. Very-high-cycle fatigue (VHCF) tests

The VHCF tests were performed by an ultrasonic fatigue testing machine with a resonance frequency of 20 ± 0.5 kHz, as shown in Fig. 4(a). Experiments were carried out under displacement control with the displacement range from 1.1 μm to 21.5 μm, which corresponds to the nominal stress amplitudes from 20 MPa to 390 MPa. The test frequency was set as 20 kHz and the stress ratio was R=−1. During the test, the specimens were cooled by compressed air to reduce the thermal effects caused by the ultrasonic frequency loading. The surface temperature of the specimen was calibrated by using thermocouples and an infrared thermal imaging camera. The volume rate of the cooling air flow was adjusted and calibrated to keep the surface temperature of the specimen at room temperature during the test.

The LPBF round bars were machined to the hourglass-shaped specimens with a minimum cross-section diameter of 3.5 mm. The geometry and dimension of the specimen are shown in Fig. 4(b). Each specimen was polished in the axial direction to reduce the influence of surface roughness on VHCF. The surface roughness of each specimen was measured by a white-light interference microscope, and the mean roughness Ra is 2.526 μm.

After the VHCF test, the fracture surfaces were observed by scanning electron microscopy (SEM). According to the SEM observations, internal defect-induced cracking was a significant failure mode for VHCF. Fig. 4(c) shows a typical fracture surface of the LPBF AlSi10Mg alloy under the VHCF loading, and the fracture surface was divided into three zones according to their features. The crack initiation zone is the smooth area in the SEM image formed by crack initiation and slow propagation. As shown in Fig. 4(c), the initiation zone includes an initial defect, and the initiation zone tends to be a circle due to the crack initiating from interior. Meanwhile, the initiation zone contains a fish-eye pattern which is a typical feature of VHCF.

The fatigue specimen was cut perpendicular to the main crack surface after the VHCF test to observe the sub-crack initiation and propagation process inside the specimen. The cutting process and the slicing section are shown in Fig. 5(a). Compared with the primary crack, the secondary crack is in the early stage of initiation and propagation. The microstructure of the defect-induced sub-cracks was investigated by using SEM, X-ray CT, and EBSD method. In the present work, an X-ray CT scanner with a resolution of 1.7 μm was used to measure the size and location of the internal defects. The maximum diameter section of the internal defects can be determined from the CT slices.

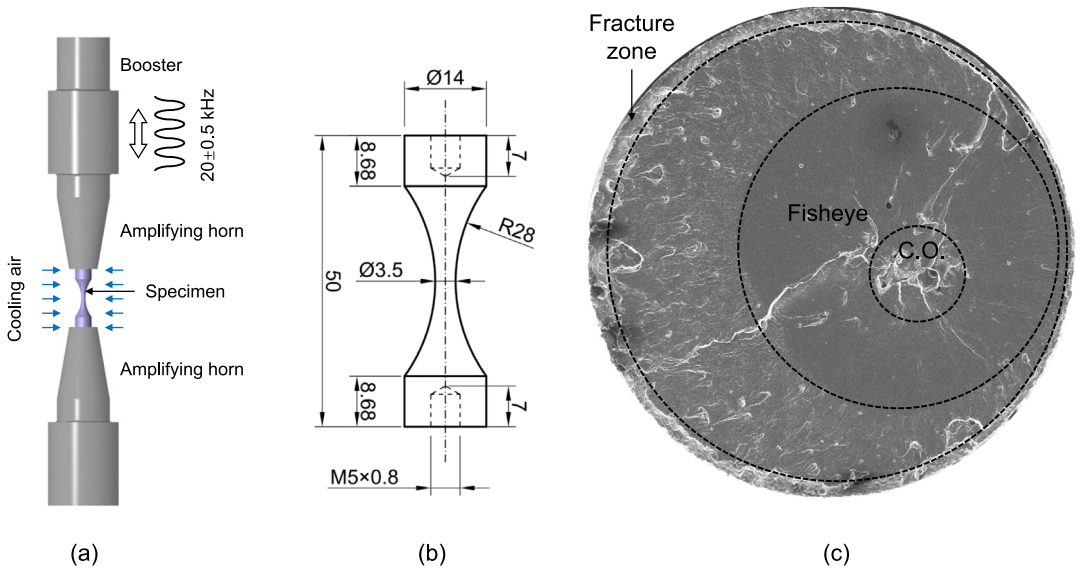

Fig. 4. (a) Ultrasonic fatigue testing device. (b) Dimensions of the hourglass specimen. (c) Fracture surface morphology of the specimen with the stress amplitude of 60 MPa and fatigue life of 3.63×10^8.

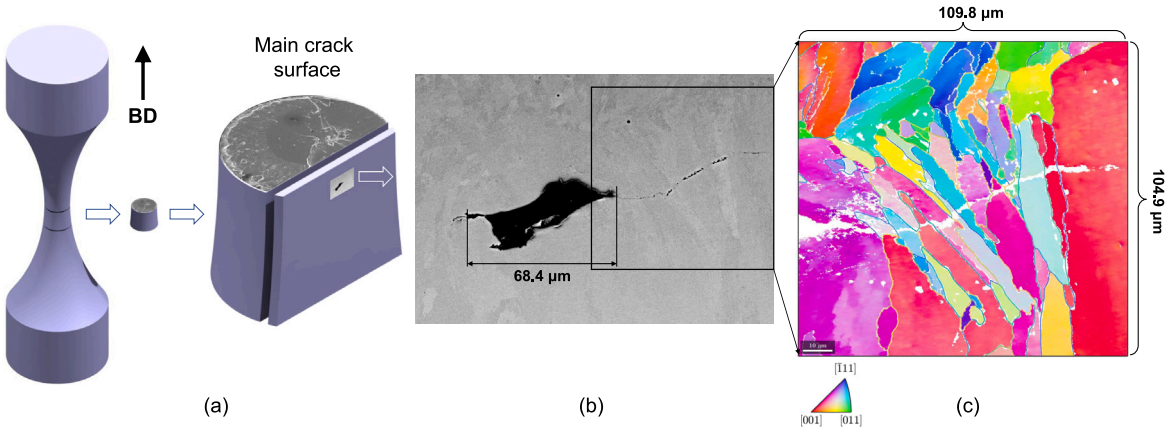

Fig. 5. (a) Cutting strategy of the failed specimen. (b) A secondary crack induced by the internal defect. (c) The EBSD inverse pole figure (IPF) map contains the internal crack.

Fig. 5(b) shows an internal defect and the sub-crack caused by the defect. The diameter of the defect is 64.8 μm, which was measured from the SEM image. Fig. 5(c) shows the EBSD inverse pole figure corresponding to the black box area in Fig. 5(b). The crack initiated from the defect during the VHCF loading. As the crack propagated, the crack would progressively grow into a circular geometry under the uni-axial high-cycle fatigue loading. The VHCF results (Qian et al., 2020) show that the cracks under the VHCF loadings mainly initiated at the core and subsurface of the specimen. The fatigue life and stress amplitude can be approximately fitted by the straight lines (Jian et al., 2021). And the porosity and defect size have a significant impact on the VHCF behavior.

3. Computations

3.1. Computational configuration

The main aim of the study is to quantitatively relate crack initiation and propagation to microstructure attributes and the competition between different fracture mechanisms. To achieve this, it is necessary to research microstructure-based fracture processes. In the study, the crystal plasticity model is used to calculate the stress–strain of the investigated microstructure under a given boundary condition. The cohesive zone model explicitly tracks the transgranular crack propagation in fully dense polycrystalline microstructures with grains. However, the current cohesive zone model cannot simulate the crack initiation with the

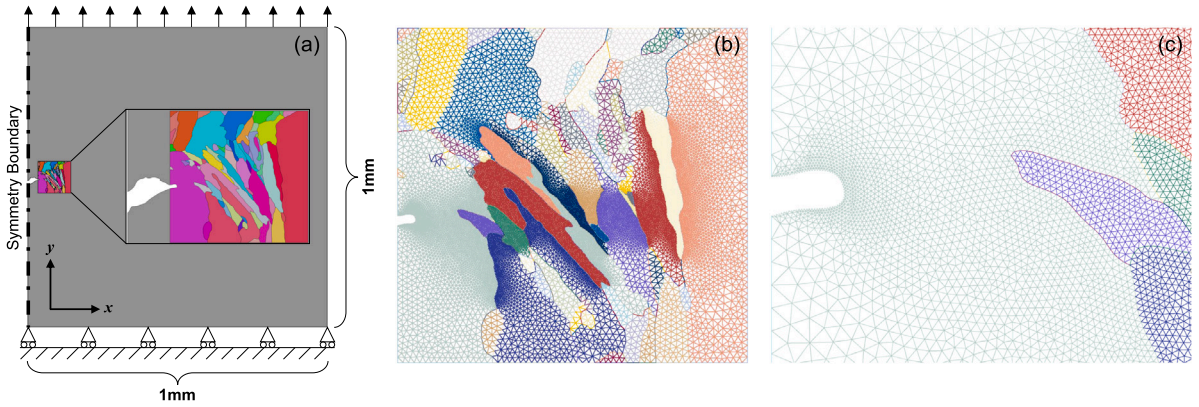

Fig. 6. (a) The microstructure-based FE model and its boundary conditions. (b) Cohesive elements net. (c) The cohesive elements at the defect edge.

stress intensity factor K lower than the threshold K_{th}. We suggested an assumption that the damage of crack initiation is a function of the local plastic strain rate of the crystal. Therefore, the computational result of the CPFEM and CZM were coupled to simulate the whole crack initiation and propagation process under the VHCF loading. Meanwhile, for the VHCF loading condition, cycle-by-cycle computation is intractable for a complex microstructure. An acceleration algorithm is proposed to improve computational efficiency while maintaining a certain level of accuracy.

3.2. Generating the finite element model from microstructure

The finite element (FE) model was created based on the EBSD data and the SEM image of defect, as shown in Fig. 6(a). To reduce the computational cost, a 2D section that contains the maximum diameter of the internal defect was selected. In the 2D model, the plane strain condition is assumed. According to existing FEM simulation (Shen et al., 2022), the stress state near the internal crack tip is the quasi-plane stress condition with stress triaxiality of around 1.5–1.7 and the Lode angle parameter of 0.7. With a high stress triaxiality value, the Lode angle effect on both strength and fracture strain is limited, therefore, the assumption of the plane stress condition in the used model should be reasonable. In addition, with a 2D model, the grain was assumed to be unlimited extension along the z thickness with its preset crystal orientation. The assumption allows the free movement of dislocations along the thickness direction within the grain region. However, the grain morphology along the thickness direction is not taken into account, and the neighboring grain (in the z direction) and grain boundary effects on dislocation movement are ignored in the model. Furthermore, the grains with diameters less than 2 μm were neglected and the grain boundaries were smoothed in the FE model construction process. The middle axis of the internal defect was set as the symmetry axis. The boundary conditions are illustrated in Fig. 6(a). Only a small region that contains the crack propagated path was configured to use the crystal plasticity model and the other region was set as the classical kinematic hardening material. During the VHCF test, the nominal stress of the specimen in the gauge section was much smaller than the yield stress of the LPBF AlSi10Mg alloy, therefore the computational accuracy of the region far from the crack tip with the classical plasticity is enough. Cohesive elements are inserted along all element sides within the crystal plastic region and no cohesive elements are used outside this region. The cohesive elements are divided into two categories: inside the grain and at the grain boundaries. They are assigned different groups of material properties according to the grain index. The net of cohesive elements is shown in Fig. 6(b). The mesh at the defect edge was refined to catch the deformation carefully, as shown in Fig. 6(c).

3.3. Theoretical framework

In this study, the crystal plasticity is coupled with the cohesive zone model that describes the fatigue damage mechanism and evolution of cracks initiation and propagation under cyclic loading.

3.3.1. Kinematics and constitutive laws of crystal plasticity

The crystal plasticity model is derived in a finite strain framework by the classical decomposition of the deformation gradient,

$$F_{ij} = F^{\mathrm{e}}_{ik} F^{\mathrm{p}}_{kj}, \tag{1}$$

where F^{e}_{ik} represents the elastic stretch and rigid body rotation and F^{p}_{kj} the plastic shears along slip planes. The plastic flow rate is associated with the superposition of all slip rates in the intermediate configuration as follows,

$$\dot{F}^{\mathrm{p}}_{ik}\left(F^{\mathrm{p}}_{kj}\right)^{-1} = \sum_{\alpha=1}^{M} \dot{\gamma}^{(\alpha)} s_i^{(\alpha)} \otimes n_j^{(\alpha)}, \tag{2}$$

where $\dot{\gamma}^{(\alpha)}$ denotes the slip rate of the α-th slip system, M is the total number of the slip systems, $s_i^{(\alpha)}$ represents the slip direction, and $n_j^{(\alpha)}$ accounts for the slip normal in the intermediate configuration. The plastic velocity gradient L_{ij}^{p} in the current configuration is defined as

$$L_{ij}^{\mathrm{p}} = F_{ik}^{\mathrm{e}} \dot{F}_{kl}^{\mathrm{p}} \left(F_{lm}^{\mathrm{p}}\right)^{-1} \left(F_{mj}^{\mathrm{e}}\right)^{-1} = F_{ik}^{\mathrm{e}} \sum_{\alpha=1}^{M} \gamma^{(\alpha)} s_k^{(\alpha)} n_m^{(\alpha)} \left(F_{mj}^{\mathrm{e}}\right)^{-1} = \sum_{\alpha=1}^{M} \gamma^{(\alpha)} s_i^{*(\alpha)} n_j^{*(\alpha)} = D_{ij}^{\mathrm{p}} + W_{ij}^{\mathrm{p}}, \tag{3}$$

where $s_i^{*(\alpha)} = F_{ik}^{\mathrm{e}} s_k^{(\alpha)}$ and $n_j^{*(\alpha)} = n_m^{(\alpha)} \left(F_{mj}^{\mathrm{e}}\right)^{-1}$ are the slip direction and normal direction in the current configuration. L_{ij}^{p} consists of a symmetric part, plastic strain rate D_{ij}^{p}, and an asymmetric part, plastic spin tensor W_{ij}^{p}. The plastic strain rate tensor and the spin tensor are described as follows:

$$D_{ij}^{\mathrm{p}} = \sum_{\alpha=1}^{M} \dot{\gamma}^{(\alpha)} P_{ij}^{(\alpha)} = \frac{1}{2} \sum_{\alpha=1}^{M} \dot{\gamma}^{(\alpha)} \left(s_i^{*(\alpha)} n_j^{*(\alpha)} + s_j^{*(\alpha)} n_i^{*(\alpha)}\right), \tag{4}$$

$$W_{ij}^{\mathrm{p}} = \sum_{\alpha=1}^{M} \dot{\gamma}^{(\alpha)} \Omega_{ij}^{(\alpha)} = \frac{1}{2} \sum_{\alpha=1}^{M} \dot{\gamma}^{(\alpha)} \left(s_i^{*(\alpha)} n_j^{*(\alpha)} - s_j^{*(\alpha)} n_i^{*(\alpha)}\right), \tag{5}$$

where the Schmid tensor denotes $P_{ij}^{(\alpha)}$, the slip spin tensor represents $\Omega_{ij}^{(\alpha)}$. Assuming that the elastic deformations of the crystal are not affected by the sliding deformation, the constitutive relationship of the crystal plasticity can be written as

$$\hat{\sigma}_{ij} = \mathbb{C}_{ijkl} D_{kl} - \sum_{\alpha=1}^{M} \left(\mathbb{C}_{ijkl} P_{kl}^{(\alpha)} + \Omega_{ik}^{(\alpha)} \sigma_{kj} - \sigma_{ik} \Omega_{kj}^{(\alpha)}\right) \dot{\gamma}^{(\alpha)}, \tag{6}$$

where $\hat{\sigma}_{ij}$ is the Jaumann rate of Cauchy stress, $\mathbb{C}_{ijkl}$ is the elastic moduli tensor. Based on Schmid's law, the slipping rate $\dot{\gamma}^{(\alpha)}$ on the α-th slip system is corresponding to the Schmid stress $\tau^{(\alpha)}$. The flow rule is suggested using a power law as:

$$\dot{\gamma}^{(\alpha)} = \dot{\gamma}_0 \left\langle \frac{\left|\tau^{(\alpha)} - \alpha^{(\alpha)}\right| - r^{(\alpha)}}{\kappa} \right\rangle^{n} \operatorname{sign}\left(\tau^{(\alpha)} - \alpha^{(\alpha)}\right), \tag{7}$$

where $\alpha^{(\alpha)}$ is the back stress, $\dot{\gamma}_0$ is the reference strain rate, $\langle \bullet \rangle$ is the Macaulay bracket, κ and n are material constants, and $r^{(\alpha)}$ is the isotropic hardening term. The rate of backstress $\alpha^{(\alpha)}$ is defined as:

$$\dot{\alpha}^{(\alpha)} = c_1 \dot{\gamma}^{(\alpha)} - c_2 \left|\dot{\gamma}^{(\alpha)}\right| \alpha^{(\alpha)}. \tag{8}$$

The evolution of isotropic hardening variable $r^{(\alpha)}$ is defined as:

$$\dot{r}^{(\alpha)} = bQ \sum_{\beta=1}^{M} h_{\alpha\beta} \left(1 - b\rho^{(\beta)}\right) \left|\dot{\gamma}^{(\beta)}\right|. \tag{9}$$

The internal state variable $\rho^{(\alpha)}$, which represents the dislocation hardening, is defined by:

$$\dot{\rho}^{(\alpha)} = \left(1 - b\rho^{(\alpha)}\right) \left|\dot{\gamma}^{(\alpha)}\right|, \tag{10}$$

where c_1, c_2, b, Q are material constants.

3.3.2. Constitutive relations of CZM

In order to model arbitrary crack propagation, cohesive elements are inserted everywhere within the microstructure region. The cohesive zone model assumes that a cohesive damage zone develops near the tip of a crack, and the traction applied on any cohesive surface T is work-conjugate to the interfacial separation θ. In the model, the free energy per unit surface of the interface is defined as

$$\psi = (1 - d)\, \psi^0, \tag{11}$$

where d represents a scalar damage variable within the range of 0 to 1. ψ^0 is the elastic energy density, which is defined as

$$\psi^0 = \frac{1}{2} \theta_i C_{ij}^0 \theta_j, \quad i, j = 1, 2, 3, \tag{12}$$

where C_{ij}^0 is the elastic tangent stiffness tensor defined as

$$C_{ij}^0 = \delta_{ij} E_{\mathrm{K}}, \tag{13}$$

where the scalar parameter E_{K} is a penalty stiffness, and δ_{ij} is the Kronecker delta. Negative values of θ_1 do not have any physical meaning because interpenetration is prevented by contact. Therefore, a modification of Eq. (12) is proposed to prevent interfacial penetration of the two adjacent layers after complete decohesion, and the proposed free energy is

$$\psi = (1 - d)\, \psi^0 - d \frac{1}{2} \delta_{1i} \langle -\theta_1 \rangle C_{ij}^0 \delta_{1j} \langle -\theta_1 \rangle, \quad i, j = 1, 2, 3, \tag{14}$$

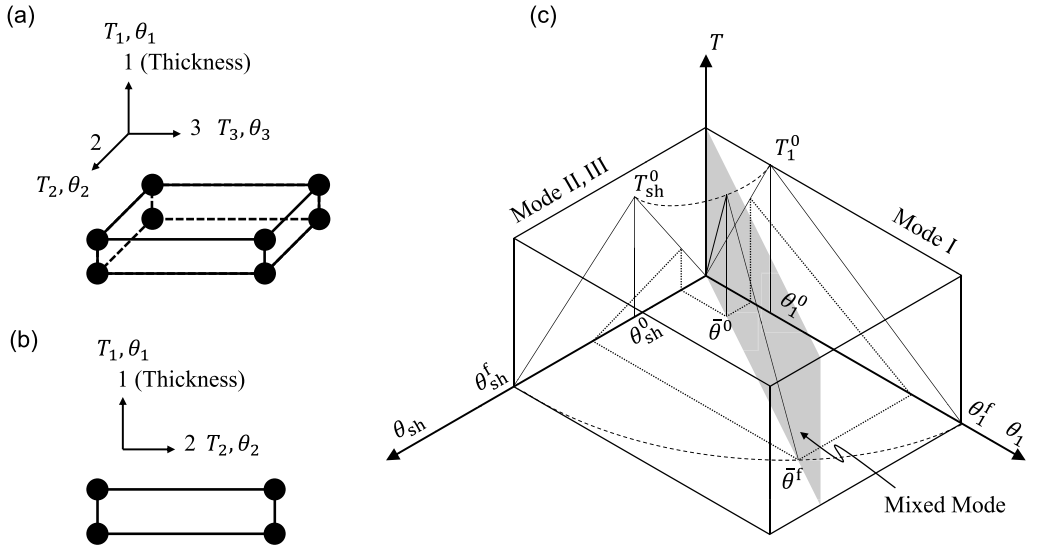

Fig. 7. (a) 3D, and (b) 2D cohesive zone elements and their local coordinates. (c) Schematic of the bilinear cohesive zone model.

where $\langle\cdot\rangle$ denotes the MacAuley bracket which defined as $\langle x\rangle = \frac{1}{2}(x + |x|)$. The constitutive relations of the CZM can be obtained by differentiating the free energy ψ with respect to the separations θ_i:

$$T_i = \frac{\partial \psi}{\partial \theta_i} = (1-d)\, C_{ij}^0 \theta_j - d C_{ij}^0 \delta_{1j} \langle -\theta_1 \rangle . \tag{15}$$

Fig. 7(a) and (b) show the 3D and 2D cohesive zone elements and their local coordinates. θ_1 and T_1 corresponding to the tension–compression direction, and θ_2, θ_3, T_2 and T_3 are used to describe the shear variable of CZM. For 2D case, $\theta_3 = 0$ and $T_3 = 0$.

3.3.3. Damage evolution of CZM

The damage evolution that results from a general loading history can be considered as the sum of the quasi-static damage, the fatigue crack initiation damage and the fatigue crack propagation damage:

$$\frac{\mathrm{d}d}{\mathrm{d}t} = \dot{d} = \dot{d}_{\text{static}} + \dot{d}_{\text{init}} + \dot{d}_{\text{prop}}. \tag{16}$$

The quasi-static damage d_{static} is the damage induced by the monotonic loading. d_{static} equals zero initially, and the damage occurs when the following criterion (Ye, 1988) is satisfied.

$$\left(\frac{\langle T_1 \rangle}{T_1^0}\right)^2 + \left(\frac{T_2}{T_2^0}\right)^2 + \left(\frac{T_3}{T_3^0}\right)^2 = 1, \tag{17}$$

where T_1^0, T_2^0, T_3^0 are the interfacial strength in the normal and tangential direction. The MacAuley bracket term $\langle T_1 \rangle$ means the pure compression does not cause any damage. For the mixed-mode damage (see Fig. 7(c)), the equivalent separation is defined as

$$\bar{\theta} = \sqrt{\langle \theta_1 \rangle^2 + (\theta_{\text{sh}})^2}, \tag{18}$$

where θ_1 is the separation in mode I, and θ_{sh} is the shear direction of the separations in mode II and in mode III:

$$\theta_{\text{sh}} = \sqrt{(\theta_2)^2 + (\theta_3)^2}. \tag{19}$$

For the bilinear cohesive zone constitutive relation shown in Fig. 7(c), the quasi-static damage d_{static} can be obtained as

$$d_{\text{static}} = \frac{\bar{\theta}^{\text{f}} \left(R_\theta - \bar{\theta}^0\right)}{R_\theta \left(\bar{\theta}^{\text{f}} - \bar{\theta}^0\right)}, \tag{20}$$

where $\bar{\theta}^{\text{f}}$ is the equivalent separation for complete failure of the interface, $\bar{\theta}^0$ is the equivalent onset displacement jump, and R_θ is a damage consistency parameter used to define loading–unloading conditions, it can be obtained as

$$R_\theta^t = \max\left\{ R_\theta^0, \max_{s\in[0,t]} \left\{\bar{\theta}^s\right\} \right\}. \tag{21}$$

In the above relation, R_θ^t represents the hitherto maximum value of the equivalent separation attained during the loading history up to the current time t (i.e., unloading does not affect this value), and R_θ^0 is an initial value.

The initiation stage of VHCF crack is mainly related to the material microstructure. Under the external cyclic load, the dislocations in the grains accumulate and gradually form the initial crack. The process of VHCF crack initiation is usually discontinuous, but in the study, an averaging treatment is used to equate the process into a slow continuous process. We assume that the crack initiation damage rate, i.e. G is close to G_{th}, is a function of the accumulated plastic strain p:

$$\dot{d}_{\text{init}} = B\left(1 - d_{\text{init}}\right)\dot{p}, \tag{22}$$

where B is a material parameter, and

$$p = \int_0^t \sqrt{\frac{2}{3} L_{ij}^{\text{p}} L_{ij}^{\text{p}}}\,\mathrm{d}s. \tag{23}$$

Because the cohesive element cannot contain the information of crystal plastic strain, the accumulated plastic strain p in Eq. (22) is obtained from its adjacent solid elements. The data transformation method between the cohesive element and solid element will be introduced in Section 3.4. From Eq. (22), it can be found that when $p = 0$, $d_{\text{init}} = 0$, and when $p = +\infty$, $d_{\text{init}} = 1$. In the present work, the evolution function of fatigue initiation damage is an assumption based on the continuum damage mechanics, and it can be improved by the deep understanding of the crack initiation mechanism.

In CZM computations, the number of fatigue loading cycles N is considered as a continuous variable. The relationship between loading time t and N can be described by

$$t = \frac{1}{f} N, \tag{24}$$

where f is the constant frequency of fatigue loadings. Based on the model proposed by Turon et al. (2007), the fatigue crack propagation damage rate $\dot{d}_{\text{prop}}$ is evaluated as follows (see Appendix A for the derivation):

$$\dot{d}_{\text{prop}} = \frac{\partial d_{\text{prop}}}{\partial t} = \frac{\partial d_{\text{prop}}}{\partial N}\frac{\partial N}{\partial t} = f\frac{1}{A_{\text{CZ}}}\frac{\left(\bar{\theta}^{\text{f}}(1-d) + \mathrm{d}\bar{\theta}^0\right)^2}{\bar{\theta}^{\text{f}}\bar{\theta}^0} C\left(\frac{\Delta G}{G_{\text{c}}}\right)^m H\left[\left(G - G_{\text{th}}\right)\left(G_{\text{c}} - G\right)\right], \tag{25}$$

where G_{c} is the fracture toughness, G_{th} is the threshold energy release rate, $H(\bullet)$ is the Heaviside step function, C and m are fatigue crack propagation parameters that must be determined experimentally. The cyclic variation of the energy release rate ΔG can be obtained by

$$\Delta G = \frac{T^0}{2}\left[\bar{\theta}^{\text{f}} - \frac{\left(\bar{\theta}^{\text{f}} - \bar{\theta}\right)^2}{\bar{\theta}^{\text{f}} - \bar{\theta}^0}\right]\left(1 - \langle R\rangle^2\right) \tag{26}$$

where R is the stress ratio. A_{CZ} denotes the area of the cohesive zone, it can be determined in 2D or 2.5D as

$$A_{\text{CZ}} = t_b \frac{\pi}{32}\frac{E G_{\text{c}}}{\left(T^0\right)^2}, \tag{27}$$

where t_b is the thickness, E is the Young's modulus, T^0 is the interfacial strength, and the parameter $\frac{\pi}{32}$ is a fitting parameter of the investigated AlSi10Mg that can be modified for other materials. If mixed-mode criteria are considered, the expressions of G_{c} and T^0 are introduced in Appendix B.

3.3.4. Backward Euler discretization

A first-order backward Euler method is used in the finite element computation. Considering the integration interval from Step t to Step $t + \Delta t$, the damage evolution of Eqs. (16) to (22) at Step $t + \Delta t$ can be discretized as follows

$$d^{t+\Delta t} = d_{\text{static}}^{t+\Delta t} + d_{\text{init}}^{t+\Delta t} + d_{\text{prop}}^{t+\Delta t}, \tag{28}$$

with the static damage at Step $t + \Delta t$ of

$$d_{\text{static}}^{t+\Delta t}\left(R_\theta\right) = \frac{\bar{\theta}^{\text{f}}\left(R_\theta^{t+\Delta t} - \bar{\theta}^0\right)}{R_\theta^{t+\Delta t}\left(\bar{\theta}^{\text{f}} - \bar{\theta}^0\right)}, \tag{29}$$

the crack initiation damage at Step $t + \Delta t$ of

$$d_{\text{init}}^{t+\Delta t}(p) = d_{\text{init}}^t + B\left(1 - d_{\text{init}}^{t+\Delta t}\right)\Delta p^{t+\Delta t}, \tag{30}$$

and the crack propagation damage at Step $t + \Delta t$ of

$$d_{\text{prop}}^{t+\Delta t}(G, \Delta G, t) = d_{\text{prop}}^t + \left(\frac{\partial d_{\text{prop}}}{\partial t}\right)^{t+\Delta t}\Delta t. \tag{31}$$

Substituting $\Delta t = \frac{1}{f}\Delta N^{t+\Delta t}$, where $\Delta N^{t+\Delta t}$ is the increment in the number of load cycles, we have

$$d_{\text{prop}}^{t+\Delta t}(G, \Delta G, N) = d_{\text{prop}}^t + \left(\frac{\partial d_{\text{prop}}}{\partial N}\right)^{t+\Delta t}\frac{\partial N}{\partial t}\frac{1}{f}\Delta N^{t+\Delta t} = d_{\text{prop}}^t + \left(\frac{\partial d_{\text{prop}}}{\partial N}\right)^{t+\Delta t}\Delta N^{t+\Delta t}, \tag{32}$$

where

$$\left(\frac{\partial d_{\text{prop}}}{\partial N}\right)^{t+\Delta t} = \frac{1}{A_{\text{CZ}}} \frac{\left[\bar{\theta}^{\text{f}}\left(1-d^{t+\Delta t}\right)+d^{t+\Delta t}\bar{\theta}^{0}\right]^{2}}{\bar{\theta}^{\text{f}}\bar{\theta}^{0}} C\left(\frac{\Delta G^{t+\Delta t}}{G_{\text{c}}}\right)^{m} H\left[\left(G^{t+\Delta t}-G_{\text{th}}\right)\left(G_{\text{c}}-G^{t+\Delta t}\right)\right], \tag{33}$$

and

$$\Delta G^{t+\Delta t} = \frac{T^{0}}{2}\left[\bar{\theta}^{\text{f}} - \frac{\left(\bar{\theta}^{\text{f}}-\bar{\theta}^{t+\Delta t}\right)^{2}}{\bar{\theta}^{\text{f}}-\bar{\theta}^{0}}\right]\left(1-\langle R\rangle^{2}\right). \tag{34}$$

Substituting Eqs. (29), (30), (32), (33) into Eq. (28), we can obtain a non-linear equation of total damage $d^{t+\Delta t}$:

$$\begin{aligned} d^{t+\Delta t} = d^{t}_{\text{prop}} + \frac{1}{A_{\text{CZ}}} \frac{\left[\bar{\theta}^{\text{f}}\left(1-d^{t+\Delta t}\right)+d^{t+\Delta t}\bar{\theta}^{0}\right]^{2}}{\bar{\theta}^{\text{f}}\bar{\theta}^{0}} C\left(\frac{\Delta G^{t+\Delta t}}{G_{\text{c}}}\right)^{m} H\left[\left(G^{t+\Delta t}-G_{\text{th}}\right)\left(G_{\text{c}}-G^{t+\Delta t}\right)\right]\Delta N^{t+\Delta t}+ \\ d^{t}_{\text{init}} + B\left(1-d^{t+\Delta t}_{\text{init}}\right)\Delta p^{t+\Delta t} + \frac{\bar{\theta}^{\text{f}}\left(R^{t+\Delta t}_{\theta}-\bar{\theta}^{0}\right)}{R^{t+\Delta t}_{\theta}\left(\bar{\theta}^{\text{f}}-\bar{\theta}^{0}\right)}. \end{aligned} \tag{35}$$

Eq. (35) can be solved once $\Delta p^{t+\Delta t}$ is determined. Meanwhile, the accumulated plastic strain at Step $t+\Delta t$ is computed by the crystal plasticity model as,

$$\Delta p^{t+\Delta t} = \Delta t\sqrt{\frac{2}{3}L^{\text{p},t+\Delta t}_{ij}L^{\text{p},t+\Delta t}_{ij}}. \tag{36}$$

The stress update algorithm and consistent material Jacobian of the crystal plasticity model are given in Appendix C. The shear strain increment at each slip system $\Delta\gamma^{(\alpha),t+\Delta t}$ is computed by the stress update algorithm iteratively, then the accumulated plastic strain $\Delta p^{t+\Delta t}$ can be easily determined by Eq. (36).

3.3.5. Acceleration strategy

Right now, the coupled CPFEM-CZM framework is ready for the cycle-by-cycle computation and can be used for the simulation of low cycle fatigue. However, the cycle-by-cycle computation is intractable for the VHCF. An acceleration strategy is necessary to improve the computational efficiency while maintaining a certain accuracy. The static damage is not accelerated in the present work. For the cyclic loading, the finite element calculation process needs to discretize the load waveform in time, and each load cycle needs at least 20 or more discretization points to describe the whole loading process well. The proposed acceleration strategy in this study can realize the approximate equivalence of load cycles under constant amplitude loading conditions, i.e., a long-period waveform is used to replace the short-period waveform in the same time period, which can greatly reduce the time increment step in the finite element computation process. The accumulated plastic strain calculated by the crystal plasticity model can realize the equivalence of load-period under constant amplitude loading conditions. Also, the propagation fatigue damage governed by the CZM model can obtain the same damage value by using a long-period waveform instead of the short-period waveform. The internal variable $\Delta p^{t+\Delta t}$, $\Delta N^{t+\Delta t}$ are accelerated by the acceleration function as:

$$\Delta N^{t+\Delta t}_{\text{acc}} = f_{\text{acc}}\left(\Delta N^{t+\Delta t}\right), \tag{37}$$

and

$$\Delta p^{t+\Delta t}_{\text{acc}} = f_{\text{acc}}\left(\Delta p^{t+\Delta t}\right), \tag{38}$$

where $f_{\text{acc}}(\bullet)$ is the acceleration function as shown in Fig. 8. The acceleration function $f_{\text{acc}}(\bullet)$ is used to scale up the value of a time or variable by a predetermined relationship.

In Eq. (32), the cyclic variation of the energy release rate $\Delta G^{t+\Delta t}$ is almost constant during thousands of loading cycles under VHCF loadings. Therefore, the term $C\left(\frac{\Delta G^{t+\Delta t}}{G_{\text{c}}}\right)^{m} H\left[\left(G-G_{\text{th}}\right)\left(G_{\text{c}}-G\right)\right]$ is considered as a constant during each computational increment. Forward Euler method is used to calculate the accelerated propagation damage as

$$d^{t+\Delta t}_{\text{prop}} = d^{t}_{\text{prop}} + \left(\frac{\partial d_{\text{prop}}}{\partial N}\right)^{t+\Delta t} f_{\text{acc}}\left(\Delta N^{t+\Delta t}\right). \tag{39}$$

To control the accuracy of simulation, a maximum increase threshold $\Delta d_{\max}$ of total damage in a computational time increment is given, and the time increment $\Delta N^{t+\Delta t}$ is controlled by

$$\Delta N^{t+\Delta t} \le f^{-1}_{\text{acc}}\left\{\frac{\Delta d_{\max}}{\max_{J}\left[\left(\frac{\partial d^{J}_{\text{prop}}}{\partial N}\right)^{t+\Delta t}\right]}\right\}, \tag{40}$$

where J is the integration points of FE-model. Once $\Delta N^{t+\Delta t}$ triggers the threshold, the computational increment will be reduced to a new smaller one and recalculated. For example, $\Delta d_{\max} = 0.001$, which means the damage evolution for an integration point is divided into at least 1000 segments. It essentially controls the acceleration period and can be altered according to desired numerical accuracy or computational cost of the approach. As the maximum increase threshold $\Delta d_{\max}$ and acceleration period $\Delta N^{t+\Delta t}$ decreases, the damage evolution law $\frac{\partial d_{\text{prop}}}{\partial N}$ obtains more accurate with more expensive computation cost. It is important to note that the

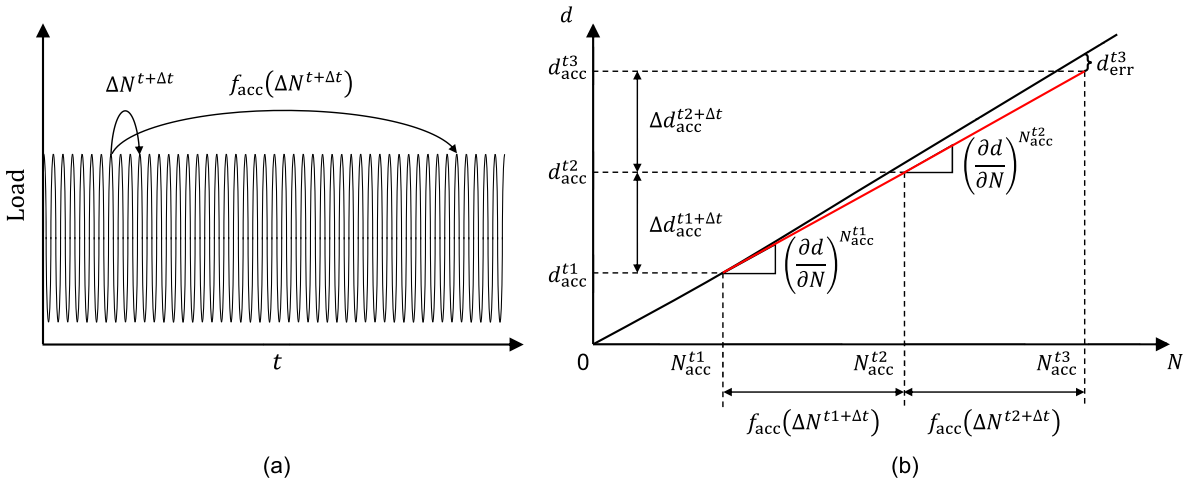

Fig. 8. Acceleration strategy: (a) cycle jump, (b) forward Euler method.

introduced CZM is rate-independent, but the crystal plasticity model is rate-dependent. The modification of load cycles can lead to additional errors in the computation of accumulated plastic strain. Fortunately, Ghisi et al. (2022) experimentally found that the LPBF AlSi10Mg did not present evident strain rate sensitivity from the strain range 0.001 s^{-1} to 1000 s^{-1}. Therefore, in this study, the crystal plasticity model is modified to be almost rate-independent by determining the rate-sensitive parameter n in Eq. (7).

For VHCF, the stress field and the crack propagation rate at the crack tip are in a steady state for a huge number of loading cycles. Zhang et al. (2022) found that the increment of the accumulated plastic strain was almost constant value in one cycle under the VHCF loading condition. In the study, a linear relation is proposed for the acceleration function as

$$f_{\mathrm{acc}}(x) = C_{\mathrm{acc}} x, \tag{41}$$

where C_{acc} is the acceleration factor. Furthermore, the acceleration function can be chosen as other forms which depend on the stability of the material during the fatigue process. And one can calibrate it by numerical calculations to achieve a better approximation.

3.4. Data transformation between the solid element and cohesive element

The coupled CPFEM-CZM is implemented into ABAQUS to solve the linear momentum balance equation under given boundary conditions in the deformed configuration. The CPFEM to solve the elastic–plastic deformation of crystals due to slip and the CZM to simulate the crack initiation and propagation are realized by UMAT subroutines. In the CPFEM UMAT, the total deformation gradient is partitioned into plastic and elastic deformation, and the equilibrium Cauchy stress σ_{ij} is obtained at the current time increment $t + \Delta t$ in an iterative way. In each iteration, the slip rate and the accumulated plastic strain are updated. In the CZM UMAT, the total damage is divided into static, initiated, and propagated damage, and the cohesive traction T_i is computed at the current time increment $t+\Delta t$ in an iterative way. In each iteration, the damage rate and equivalent separation are updated. The crack initiation damage rate $\dot{d}_{\mathrm{init}}$ requires the non-local information including the field variable at neighboring material points, which is unavailable in UMAT. Therefore, a common data field was generated to store and transfer the non-local information.

Since cohesive elements are not continuum elements, the accumulated plastic strain cannot be calculated within the cohesive element itself. Therefore, the accumulated plastic strain of the cohesive parameters is achieved by a coupling of the cohesive elements to the adjacent solid elements. The values of the internal variable from the continuum elements computed from the CPFEM are transferred to the corresponding cohesive element. In the present work, only the two-dimensional case is considered, and the element types used in the simulations include the 3-node triangular element, the 4-node quadrilateral element, and the 4-node cohesive element. The number and location of integration points for each type of element are shown in Fig. 10. Meanwhile, Fig. 10 shows the rules for data transferring from the continuum elements to the cohesive elements. If a cohesive element is adjacent to a quadrilateral element, the two integration points of the cohesive element read the data of their closest integration point in the quadrilateral element.

The converged Cauchy stress σ_{ij} and cohesive traction T_i obtained in one iteration are used to update the nodal displacements. Once the nodal displacements converge, the updated accumulated crystal plastic strain will be stored in the common data field by the user subroutine UVARM, as shown in Fig. 9. Finally, the equilibrium stress, the elastic and plastic deformation, the internal state variables describing the plastic deformation, the equivalent displacement jump, the cohesive traction and the cohesive damages for each increment are obtained.

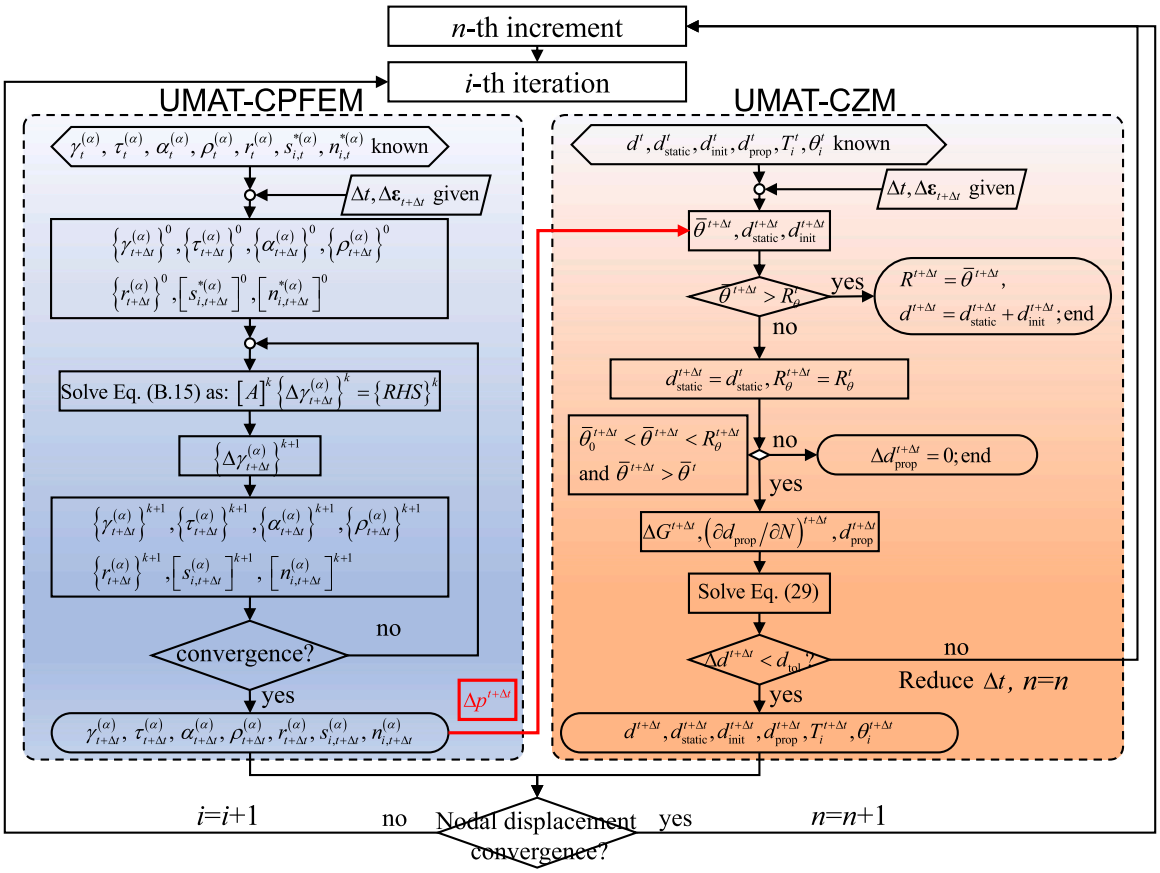

Fig. 9. Flow chart of the time integration scheme for the coupled CPFEM with CZM. *i* refers to the *i*th call for UMAT in *n*th increment.

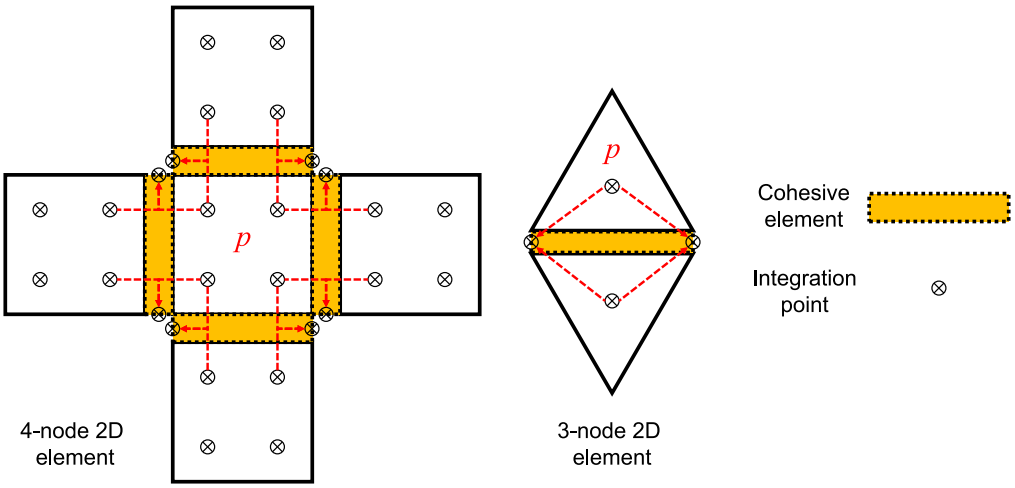

Fig. 10. Schematic illustration of internal variable value being transferred to cohesive elements from their adjacent solid elements.

3.5. Parameters

3.5.1. Parameters of crystal plasticity model

The crystal structure of the LPBF AlSi10Mg alloy is the face-centered cubic (FCC). At room temperature, its main slip system leading to the plastic deformation is the octahedral slip system {111}< 011>. Uni-axial tensile tests were carried out to determine

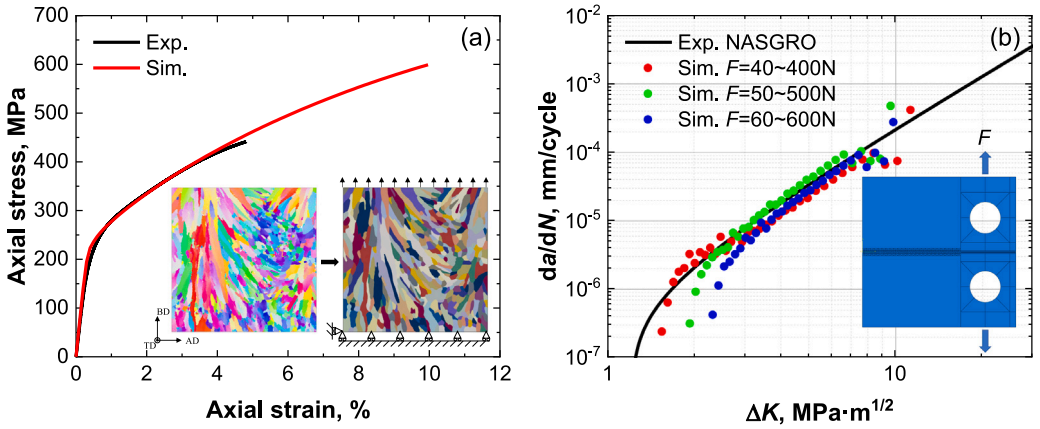

Fig. 11. Comparison of experimental and computational results with (a) the microstructure-based tensile model and (b) cyclic crack extension model of CT specimen.

Table 3
The material parameters of the crystal plasticity model of the investigated AlSi10Mg alloy.

Material parameters	Octahedral slip system {111}<011>
Elastic constants $E_{crystal,11}$, MPa	100731
Elastic constants $E_{crystal,12}$, MPa	60345
Elastic constants $E_{crystal,44}$, MPa	30087
Reference strain rate $\dot{\gamma}_0$, s^{-1}	0.001
n	10
κ, MPa	82
Kinematic hardening, c_1	2300
Kinematic hardening, c_2	10
Isotropic hardening, b	1
Isotropic hardening, Q, MPa	100

and validate the parameters of the crystal plasticity model. A 2D finite element RVE model of the investigated alloy was generated from the EBSD data by our developed python programs, as shown in Fig. 11(a). Both the height and width of the model were 245 μm. The tensile direction is the building direction. The FE model was meshed by the four-node plane strain element, and the total number of elements is about 55000. To avoid rigid body motion, the node in the bottom-left corner was limited in the BD and AD directions. Corresponding to the tensile tests, a uni-axial load was applied at the upper border of the model along the build direction with a strain rate of 0.001 s^{-1}. By using the trial-error optimization method, the parameters of the crystal plasticity model of the investigated AlSi10Mg alloy are determined and listed in Table 3. The comparison of the experimental and computational results are shown in Fig. 11(a). The computational results have a good agreement with the tensile test.

3.5.2. Parameters of cohesive zone model

The parameters of cohesive zone model were determined by crack extension tests with standard CT specimens. According to the previous work (Zhang et al., 2022), we obtained the basic elastic–plastic parameters of the LPBF AlSi10Mg alloy, as listed in Table 4. In the CZM, the unit stiffness E_K is suggested to be set much larger than the elastic modulus in order to reduce the effect of cohesive elements on material stiffness. However, a too large value of E_K will reduce the convergence performance of the whole model. According to the parametric study, we take $E_K = 650000$ N/mm^3. In the present work, the traction strength, T_1^0, T_2^0, T_3^0 were assumed to equal the ultimate tensile strength σ_u of 465 MPa. The fracture toughness of the LPBF AlSi10Mg is from 27 to 31 MPa ($\sqrt{m}$), and the critical fracture energy G_{Ic} is around 10 N/mm (Paul et al., 2021). G_{IIc} and G_{IIIc} are usually lower than G_{Ic}, so we assume that both G_{IIc} and G_{IIIc} are 8 N/mm. According to the bilinear relationship, when the critical fracture energy and traction strength are given, the separation values are determined while the material is completely damaged. The parameters C and m in Eq. (A.6) describing the crack propagation behavior can be determined from the crack extension experiment results. The parameter B in Eq. (22) is used to control the proportion of initiation damage in the total damage. Because B is difficult to determine by experiments directly, the value of B is set by the assumption and numerical validation. A finite element model of the CT specimen was generated and the cohesive element was inserted at the crack surface as shown in Fig. 11(b). Taking the experimental NASGRO relation (Qian et al., 2022) of the LPBF AlSi10Mg alloy as the target curve, we used a trial-error method to optimize the values of the cohesive parameters. Fig. 11(b) shows that the computational results have a good agreement with the experimental NASGRO relation. All of the cohesive parameters of the cohesive zone model are listed in Table 5.

Table 4
Elastic–plastic parameters of the cohesive zone model.

E_{11}, MPa	E_{22}, MPa	G_{12}, MPa	ν_{12}	σ_y, MPa	σ_u, MPa
65000	65000	25000	0.3	280	465

Table 5
Cohesive parameters of the cohesive zone model.

E_K N/mm^3	T_1^0 MPa	T_2^0 MPa	T_3^0 MPa	G_{Ic} N/mm	G_{IIc} N/mm	G_{IIIc} N/mm	C mm/cycle	m	B	C_{acc}
6500000	465	465	465	10	8	8	2.1×10^{-5}	2.51	1.6×10^{-5}	1.0×10^{5}

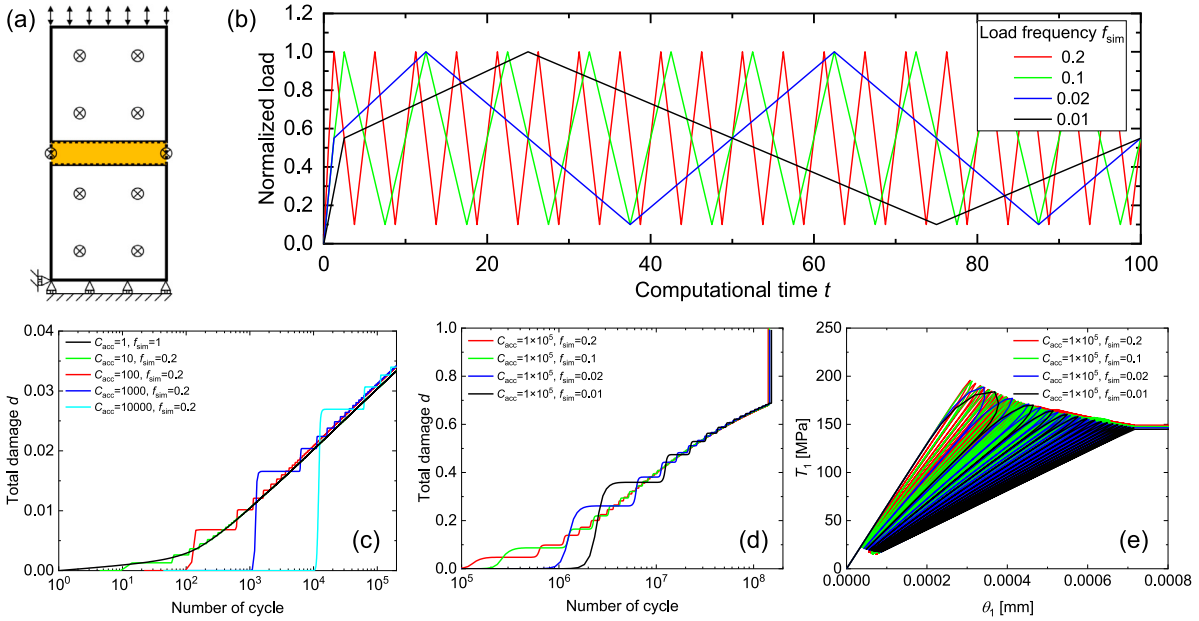

Fig. 12. (a) Basic FE-model for validation. (b) Loads with the same amplitude but different frequencies. (c) Total damage of Examples 1 to 5. (d) Total damage of Examples 6 to 9. (e) Traction-separation responses of Examples 6 to 9.

4. Discussion

4.1. Validation of the CPFEM-CZM model and the acceleration strategy

The framework of the CPFEM-CZM model and its implementation method are introduced in Section 3. A numerical verification of the proposed CPFEM-CZM model is firstly studied with a plane strain FE model which contains two solid elements of crystal plasticity and one cohesive element, as shown in Fig. 12(a). The crystal orientations of the two solid elements are the same, and their crystal axis < 001>, < 010>, < 100> are in the direction of axis x, y, z of the global Cartesian coordinate. The whole model is subjected to cyclic fatigue loading. The validity of the acceleration algorithm is based on two criteria: firstly, the damage value obtained from a long-period waveform computation should be the same as that obtained from a short-period waveform within the same time period; secondly, the damage value obtained with different acceleration factors should be the same as that obtained without acceleration.

The VHCF tests for the LPBF AlSi10Mg were carried out with a constant frequency of f_{exp} = 20 kHz, and each cycle lasted for 5×10^{-4} s. Since AlSi10Mg exhibits rate-independent behavior, altering the loading frequency has minimal impact on the simulation results. Therefore, we designated the reference computational loading frequency as f_{ref} = 1, i.e. $t = N$, for easy conversion between loading time and the number of cycles. According to Eqs. (24), (37) and (41), the calculated number of cycles N_{acc}, computational time t, and acceleration factor C_{acc} have the following relation:

$$N_{acc} = C_{acc}N = C_{acc}f_{ref}t = C_{acc}t. \tag{42}$$

It is important to note that the aforementioned relationship only applies to a constant load frequency, and if f_{ref} is not equal to 1, a frequency correction factor between t and N must be included in the CZM UMAT subroutine.

Triangular waves with the same amplitude and stress ratio but different load frequencies f_{sim} were used as the boundary conditions for the current numerical test model. The waveforms with load frequencies of 0.2, 0.1, 0.02, and 0.01 are shown in

Table 6
Parameters for numerical testing to validate the CPFEM-CZM model.

Example	C_{acc}	Load frequency f_{sim}	Computational time t	Number of cycles $N_{acc} = C_{acc}t$
1	1.0×10^0	1	2×10^5	2×10^5
2	1.0×10^1	0.2	2×10^4	2×10^5
3	1.0×10^2	0.2	2×10^3	2×10^5
4	1.0×10^3	0.2	2×10^2	2×10^5
5	1.0×10^4	0.2	2×10^1	2×10^5
6	1.0×10^5	0.2	2×10^3	2×10^8
7	1.0×10^5	0.1	2×10^3	2×10^8
8	1.0×10^5	0.02	2×10^3	2×10^8
9	1.0×10^5	0.01	2×10^3	2×10^8

Fig. 12(b), while the waveform with $f_{sim} = 1$ is not presented in the figure due to its overly dense lines. This article provides a total of nine numerical validation examples with different parameters, including six different acceleration factors C_{acc}: 1, 10, 100, 1000, 10000, and 100000. The parameter combinations are listed in Table 6. Example 1 is in an unaccelerated state with an acceleration factor C_{acc} of 1 and a loading period of 1. Due to the limited number of elements in the finite element model (only 3), parallel computing acceleration is difficult, and only 2×10^5 cycles were computed. Fig. 12(c) illustrates the comparison of total damage between Examples 2 to 5 and Example 1. It indicates that the total damage computed using the acceleration method is nearly identical to the unaccelerated computation. The results demonstrate that a relatively accurate estimate can be achieved for a wide range of acceleration coefficients during a given number of load cycles. However, as the acceleration coefficient is derived using the forward Euler method, the error will gradually accumulate as the load cycle progresses. Nonetheless, we can calibrate the model parameters associated with a specific acceleration coefficient using CT crack extension tests. This approach ensures that the current acceleration coefficient and its corresponding material parameters better align with the experimental results.

The acceleration factor, C_{acc}, for Examples 6 to 9, is fixed at 1.0×10^5, while the total computational time t is kept constant at 2.0×10^3, which corresponds to a total number of 2.0×10^8 cycles. However, the load frequencies for Examples 6 to 9 vary, being set to 0.2, 0.1, 0.02, and 0.01, respectively, as listed in Table 6. Fig. 12(d) displays the total damage for Examples 6 to 9, while Fig. 12(e) shows the traction-separation behavior of the cohesive element in Examples 6 to 9. The numerical results demonstrate that the damage values obtained from long-period and short-period waveform computations are nearly identical within the same computational time. Additionally, the acceleration method is convergent as the computational load frequency f_{sim} approaches the reference frequency f_{ref}. Therefore, we can achieve a balance between accuracy and efficiency by choosing the appropriate computational load frequency f_{sim} to accelerate the model. In practical VHCF simulations, the stress levels are low enough that very large acceleration factor C_{acc} and low load frequency f_{sim} can usually be achieved to accelerate the calculations.

To summarize, the proposed VHCF acceleration method involves two main steps. Firstly, the forward Euler method and the acceleration factor are applied to scale the number of cycles. Secondly, by replacing high-frequency loads with low-frequency loads, the number of waveform scatterings of cyclic loads in finite element calculations is reduced. This approach can significantly improve the efficiency of VHCF simulations. The effectiveness of this proposed acceleration method is verified through numerical examples.

4.2. Analysis of model parameters

In the present work, the damage of the cohesive element was divided into three parts: d_{static}, d_{init}, and d_{prop}. d_{static} is the damage induced by the monotonic loading, which is not the main topic of the current study. d_{prop} is the damage in the crack propagation stage and d_{init} is used to describe the damage in the crack initiation stage. The evolution of d_{prop} is related to the long crack propagation, which is validated in Section 3.5.2. It can well describe the process and rate of crack propagation in Stage II. Parameters C and m in Eq. (32) are used to describe the crack propagation behavior of Stage II. Therefore, the values of C and m have to be determined to fit the results of the crack propagation tests. Fig. 11(b) shows that the computational results of CT specimen have a good agreement with the experimental results.

The evolution of d_{init} with the acceleration coefficient C_{acc} is proposed as Eq. (30). The initiation damage d_{init} is a monotonic function and its rate is proportional to the rate of accumulated shear strain $\dot{p}$. As written in Eq. (22), B is the parameter to control the crack initiation process. Fig. 13 shows the damage and cohesive traction-separation of the proposed CPFEM-CZM model under the same boundary condition but with different model parameter B, by using the FE-model in Fig. 12(a). In the crack growth Stage I ($\theta_1 < \theta_{th}$), the evolution of d_{prop} is inactive, and the total damage d is equal to the initiation damage d_{init}, where θ_{th} is the separation related to the G_{th}. The element stress level is much lower than the critical traction T_1^0, as shown in Fig. 13(g). The stiffness of the element decreases slowly with the accumulation of damage.

As the initiation damage increases, when $\theta_1 \geq \theta_{th}$, the fatigue crack propagation enters Stage II. The evolution of d_{prop} is written in Eq. (32). Fig. 13 shows that the larger the value of B, the faster the damage rate caused by the accumulated plastic strain p. By changing the value of B, one can control the proportion of the first stage of crack extension in the total damage.

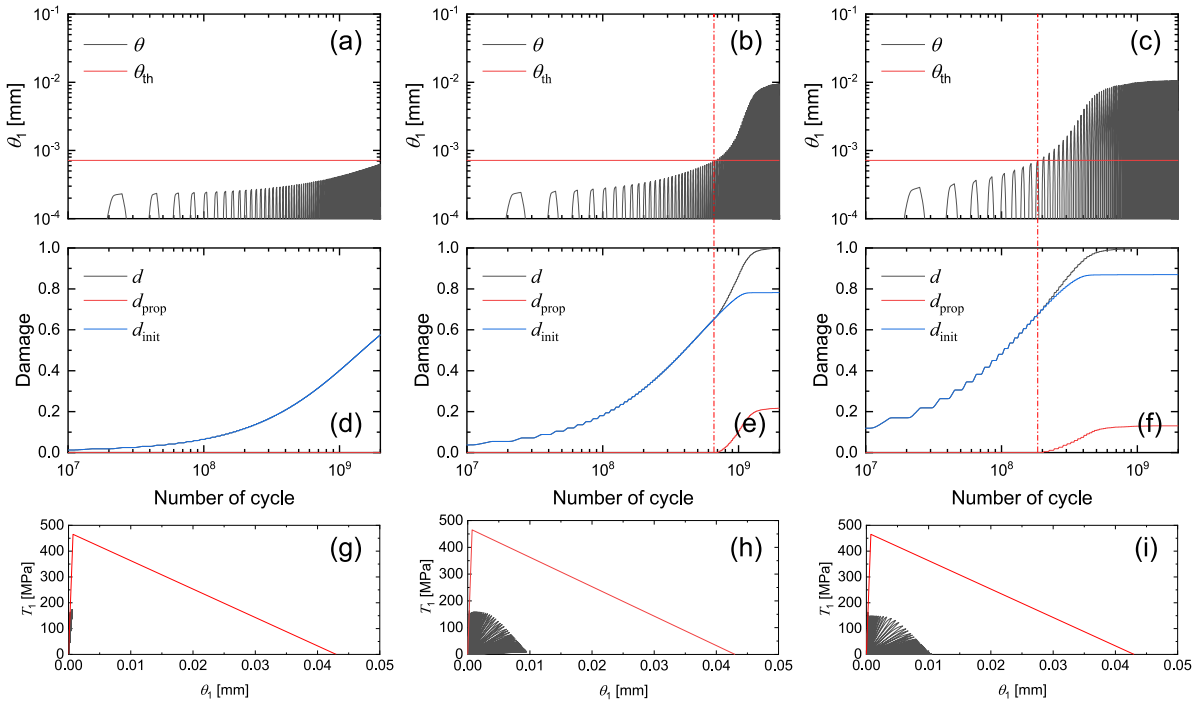

Fig. 13. Damage evolution and cohesive separation of the proposed CPFEM-CZM model under the same boundary condition but different model parameters: (a), (d), (g) $B = 1 \times 10^{-6}$, (b), (e), (f) $B = 3 \times 10^{-6}$, (c), (f), (i) $B = 1 \times 10^{-5}$.

4.3. Comparison of computational and experimental results for the LPBF AlSi10Mg alloy under VHCF

The theoretical framework has been introduced in Section 3 and its parameters are validated in Section 4.1. In this section, the EBSD mapped FE-model shown in Fig. 6 is simulated by using the proposed framework with the validated parameters. The VHCF boundary conditions in the FE-model are set to the same values as those in the experiment, with a stress amplitude of 60 MPa and a stress ratio of −1. The computational results are compared to the experimental ones in the following four topics. Firstly, the accumulative plastic deformation is compared with the EBSD result, and fine grains are corresponding to the large accumulative plastic deformation on the crack surface. Secondly, damage evolution and crack initiation are studied, and the crack initiation mechanism of the proposed framework is the primary issue in the VHCF. Thirdly, the stress distribution at the crack tip is analyzed to consider the crack closure behavior in the VHCF. Finally, the computational VHCF crack growth rate is compared with the experimental ones, to validate the effectiveness of the coupled CPFEM-CZM model and the acceleration method.

4.3.1. Accumulative plastic deformation and local fine grains

The accumulative plastic deformation and microstructure evolution by the computational framework are studied. Fig. 14 shows the experimental and computational results of the LPBF AlSi10Mg alloy under VHCF loading. Fine grains, which is a characteristic feature of VHCF (Pan et al., 2021), were experimentally observed at the crack surface as shown in Fig. 14(a). Hong et al. (2016) proposed a numerous cyclic pressing (NCP) model on the formation mechanism of the fine grain area induced during VHCF. The NCP model concluded that the fine grain formation because of the repeated contact stress between the crack surfaces and a sufficient number of tension–compression loading cycles experienced during VHCF. The present calculation results confirm the validity of the NCP assumption where the local stress concentration leads to a large cumulative plastic strain due to the tortuous structure of the crack surface as shown in Fig. 14(c).

A kernel average misorientation (KAM) map based on EBSD is shown in Fig. 14(b). The high KAM value corresponds to large plastic deformation sites. The high KAM location in Fig. 14(b) is close to the defect, because the crack growth rate is slower near the defect and the material undergoes more fatigue cycles compared to the cracked surface away from the defect. Correspondingly, Fig. 14(c) is the computational accumulated plastic strain map under an equivalent loading cycle of 3.27×10^8. Grains near the crack surface are distinctive with undergoing larger plastic strain than the other grains. The crack occurs from the edge of the defect as a result of large local deformation. Comparing the results of Fig. 14(b) and Fig. 14(c), there is a good agreement between the calculated accumulative plastic strain and KAM values.

Grain orientations also have an essential influence on the computational deformation consistency and accumulative plastic strain. In this study, the grain orientations were measured by the EBSD method, and the misorientation at the grain boundaries was calculated and plotted in Fig. 15(a). According to the symmetry of the FCC metal, the available grain boundary misorientations

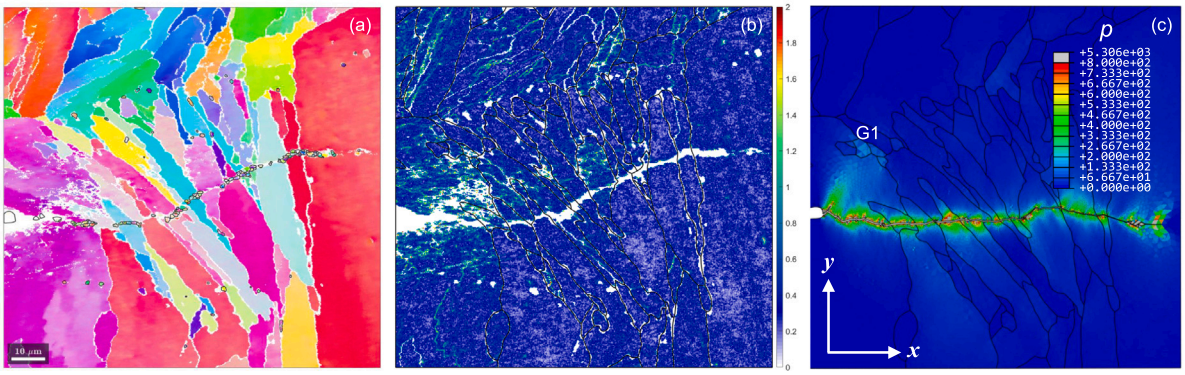

Fig. 14. (a) Fine grains at crack surface. (b) KAM map. (c) Computational result of investigated area.

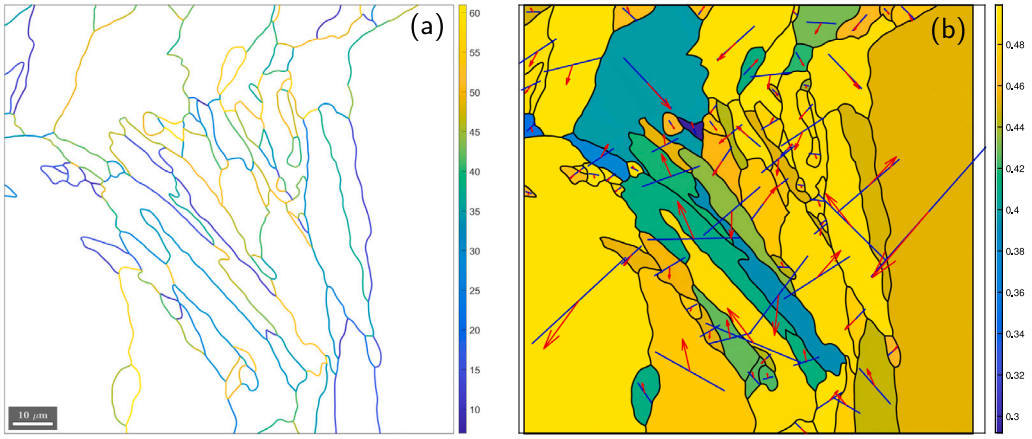

Fig. 15. (a) Misorientation angle of grains and (b) Schmid factor of {111}< 110> slip system under vertical loading.

are in the range from 0° to 62.8°. By comparing Fig. 14(b), Fig. 14(c) and Fig. 15(a), the large deformation and high KAM value usually occur near the grain boundaries, corresponding to the misorientation angles between 30° and 60°. The reason is that large angular grain boundaries are more susceptible to deformation incoherence resulting in local deformation concentration.

The Schmid factor for {111}< 110> slip system of the investigated microstructure was shown in Fig. 15(b), corresponding to the VHCF loading in vertical direction. The blue line in each crystal is the intersection line of the slip plane and BD-RD plane, and the red arrow represents the projection of the slip direction on the BD-RD plane. According to Schmid law, the larger the Schmid factor, the greater the effective critical resolved shear stress, and the corresponding slip system will be easily activated. By comparing the accumulated plastic strain in Fig. 14(c) with the Schmid factor in Fig. 15(b), it is observed that the shear band usually occurs in the grain with large Schmid factors. Moreover, the grains with small Schmid factors are corresponding to small accumulated plastic strain, such as the grain G1. It can be demonstrated that local plastic deformation during VHCF attributes to slip system {111}< 110> activation, which confirms that the proposed computational framework is sensitive at the grain scale. On the other hand, the computational result indicates that crack propagation exhibits transgranular fracture, which coincides well with experimental observations. The experimental results show that the crack is deflected in the middle of the investigated region. The reason for the deflection is that the crack expansion process is influenced by adjacent defects in the three-dimensional structure. The crack deflection is another research topic which is not discussed in the current article. The current numerical computation process in which the crack expands perpendicular to the load direction cannot simulate this deflection process in the large region, which requires more careful 3D study.

4.3.2. Damage evolution and crack initiation

In this part, the crack initiation and damage evolution during VHCF are studied. As introduced in Section 3.2, the FE-model is constructed by the solid elements and the cohesive elements net between each pair of adjacent solid elements (see Fig. 6). The calculated crack initiation at the defect edge is the result of the combination of plastic deformation described by crystal plasticity and the damage governed by cohesion zone model. As aforementioned, the activated dislocation system under a certain loading condition based on the grain orientation can be calculated according to the Schmid law. As shown in Fig. 15(b), for the grain near the defect edge, if the uniaxial tension along y direction is assumed, its activated dislocation slip system should be {-111}< 0-11>.

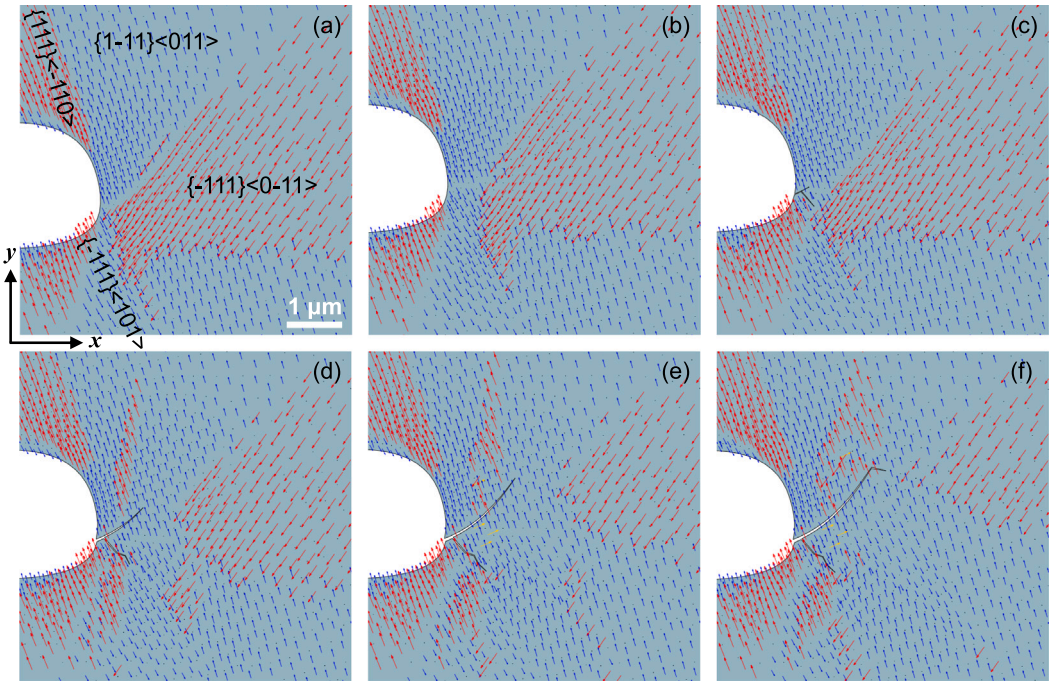

Fig. 16. Main active dislocation slip directions from simulation at (a) $N = 1 \times 10^4$, (b) $N = 5 \times 10^5$, (c) $N = 2.5 \times 10^6$, (d) $N = 4.5 \times 10^6$, (e) $N = 6.5 \times 10^6$, and (f) $N = 8.5 \times 10^6$.

However, the internal defects lead to local redistribution of stresses, and the activated slip direction is also changed in the region around the defect. The maximum shear strain rate of the FCC crystal slip system is defined as

$$|\dot{\gamma}|_{\max} = \max_{1 \le \alpha \le M} \left| \dot{\gamma}^{(\alpha)} \right|. \tag{43}$$

The main active slip direction is defined as the slip direction corresponding to the maximum shear strain rate $|\dot{\gamma}|_{\max}$. The main active slip directions at the crack initiation location are presented in Fig. 16. Fig. 16(a) shows that, at $N = 1 \times 10^4$, even with a small global plastic deformation, the stress state has been changed due to the defect morphology, leading to a distinct change of the main active slip systems in the region near the defect edge, by comparing to Fig. 15(b). There are 4 main slip directions in this region as {111}<-110>, {1-11}< 011>, {-111}< 0-11>, and {-111}< 101>. Cracks initiated at the interface of different main slip orientation regions, such as {-111}< 0-11> with {1-11}< 011> and {-111}< 0-11> with {1-11}< 101>. The elements at the interface of different main slip orientation regions produce more accumulated plastic strain p than the other elements during the simulation. Therefore, the initiation damage value d_{init} of their corresponding cohesive elements is larger than the other regions, and the crack initiated at the location of these cohesive elements. Fig. 16(b) to (f) show that the main active slip directions change as the growth of the crack, and the variation causes the next deflection of the crack. It is concluded that the simulated tortuous crack path was related to the crystallographic slip systems within which the slip value is the largest. It is consistent with the phenomena observed by Karamitros et al. (2022) in the crack path of an FCC single crystal alloy.

The value of damage variable d is within the range of 0 to 1. When $d = 0$, no damage occurs in the cohesive element. When $d = 1$, the cohesive element is totally damaged. Near the defect edges, the cohesive elements within different ranges of damage value are plotted in Fig. 17, at the number of cycles $N = 8.5 \times 10^6$. It is clear that the final crack path is along the cohesive elements with larger damage values. Fig. 17(f) is the finally computed crack path, corresponding to the $d = 1$. Fig. 17(a) to (e) shows that the damage occurs in many cohesive elements around the defect edges during the simulation. As the cohesive zone element at the crack path wins the competition for damage evolution, the cohesive zone elements near the newly generated crack surface stop undergoing damage due to local stress unloading. More interestingly, with the overlapping of the final crack propagation pattern and the dislocation slip direction maps (Fig. 16), it is seen that the crack propagation direction has been affected by the dislocation slip direction. Within a grain region with the same crystal orientation, the main activation dislocation slip directions have been divided into different regions. With further loading and crack initiation, the stress states in the critical damage region become more complex, and the main active dislocation slip system as well as slip directions are also changed accordingly. However, the initial slip direction has an indelible influence on the crack behavior. The crack propagation path tends to be along the region with the dislocation slip direction difference. There might be two reasons. First, due to the slip direction difference in neighbor elements, the dislocation slip in these regions would be restricted and the local dislocation walls might be formed. Secondly, due to the different slip directions in these sub-grain regions, the evolution of crystal orientations would also be varied and lead to the formation of

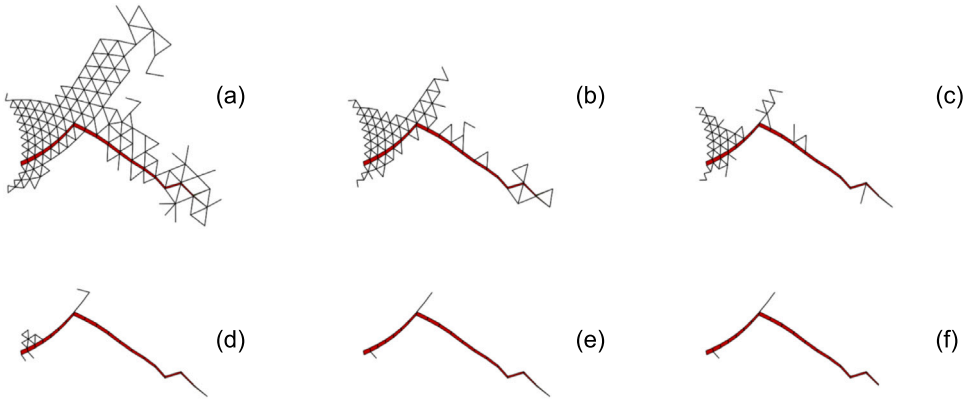

Fig. 17. Cohesive elements within the damage range of (a) $d > 0.2$, (b) $d > 0.3$, (c) $d > 0.4$, (d) $d > 0.5$, (e) $d > 0.6$, and (f) $d = 1.0$.

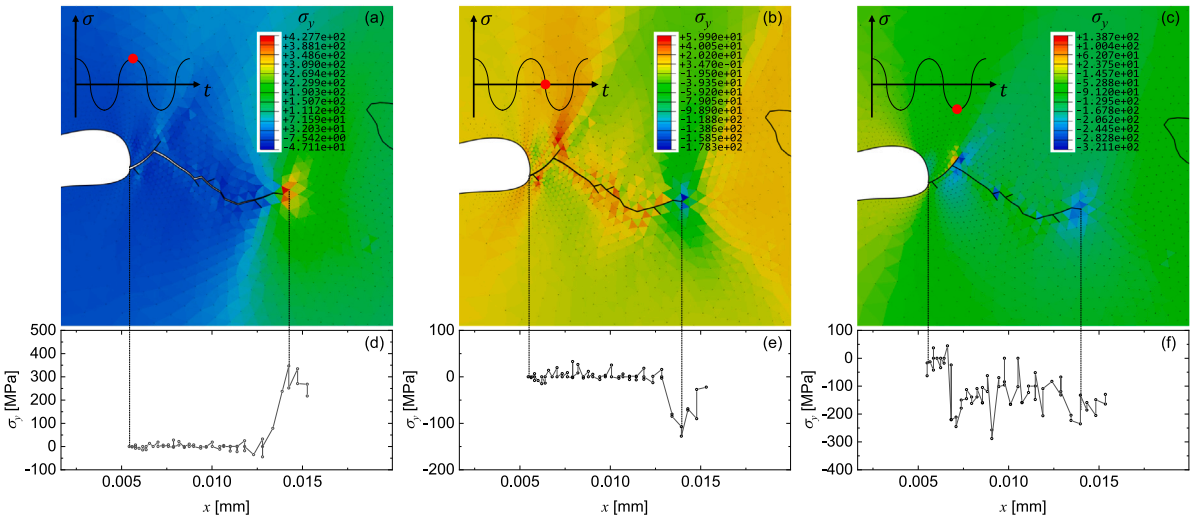

Fig. 18. Axial stress distribution at the defect-induced crack tip at (a), (d) maximum tension, (b), (e) mean load, and (c), (f) maximum compression.

the sub-grain structure. Those sub-grain cell boundaries would be the constraint plastic deformation region. Correspondingly, the damage accumulates faster in the interaction regions with different dislocation slip systems, and these regions become the damage initial zone and final crack path in the 2D simulation.

4.3.3. Stress distribution at the crack tip

Stress distributions at the crack tip have a significant influence on the crack growth. Fig. 18 shows the axial stress distribution along the crack path, corresponding to the crack length of 8.4 μm. The crack is in Stage I of VHCF. At the moment of maximum tension, the axial stress at the crack face is almost zero, as shown in Fig. 18(a) and (d). The front of crack tip is a tiny plastic region of tension stress state with a size of 2 μm. The maximum axial stress at the maximum tension moment is less than T_1^0 of 465 MPa. Therefore, no quasi-static damage currently occurs during the VHCF loading. Fig. 18(b) and (e) show the axial stress distribution at the zero load moment. The axial stress along the crack path indicates that only the crack tip region is closed at this moment. A compression stress region located at the front of crack tip due to accumulated plastic strain is responsible for the crack closure effect. Fig. 18(c) and (f) show the axial stress along the crack path under the maximum compressive load, and the entire crack surface is in a closed state. The pressure distribution on the crack surface is not uniform, and stress concentration occurs at the turning region of the crack. The inserted cohesion elements net does not affect the material stiffness due to the very high cohesive element stiffness E_K. The computational stress distributions at the crack tip which are calculated by the current framework are in good agreement with the analytical solution and traditional FE computations. Meanwhile, the damage of the cohesive zone elements is based on the energy criterion, which can effectively avoid the local effect of the damage due to the small mesh size.

4.3.4. Crack growth rate

In this section, the calculated crack growth rate is analyzed. Fig. 19(a) shows the evolution of computational crack length with fatigue cycles. The crack length a was defined as crack projection in the direction perpendicular to the loading axis including

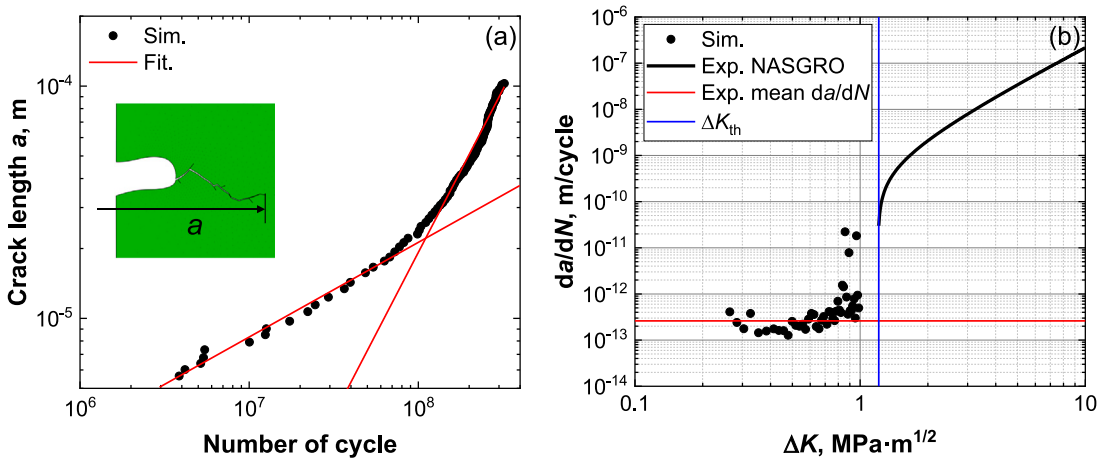

Fig. 19. (a) Simulated crack length v.s. number of cycle, and (b) VHCF crack growth rate.

the defect size. The crack length grows with the increasing number of loading cycles, which shows a bilinear relationship in the logarithmic coordinate. The rate of crack propagation increases as the crack length increases. The reason is that the proportion of d_{prop} damage increases in the total damage during the simulation as the crack length increases. Therefore, the parameter B can also control the acceleration point of the crack growth rate.

With regard to VHCF, we should note that the fundamentals of the mechanics of fatigue thresholds in that the threshold stress intensity factor range ΔK_{th} for small cracks is not constant and is not identical with the values of ΔK_{th} for long cracks. Murakami (2019) introduced the threshold stress intensity factor range of small crack with stress ratio R=−1 for internal defects:

$$\Delta K_{\text{th}} = 2.77 \times 10^{-3} \left(H_{\text{V}} + 120\right) \left(\sqrt{A}\right)^{1/3}, \tag{44}$$

where the units are ΔK_{th}: MPa $\text{m}^{1/2}$, H_{V} (Vickers hardness): kgf/mm^2, $\sqrt{A}$ (crack equivalent diameter): μm. The average Vickers hardness H_{V} of the investigated LPBF AlSi10Mg was measured as 132 kgf/mm^2, and the square root of the internal defect area is 60.6 μm. Therefore, the threshold stress intensity factor range ΔK_{th} is predicted by Eq. (44) as 2.74 MPa $\text{m}^{1/2}$. Furthermore, the ΔK_{th} of LPBF AlSi10Mg was also measured experimentally by Zhang et al. (2022) with standard CT specimens as 1.21 MPa $\text{m}^{1/2}$. Fig. 19(b) shows the simulated crack growth rate $\text{d}a/\text{d}N$ versus the stress intensity factor range ΔK. The investigated VHCF crack was initiated at the internal defect of the specimen. It is unlikely to establish a proper in-situ observation method to measure the whole crack growth process of the internal crack. The crack was found by slicing the material after the fatigue test, so we can only obtain its average propagation rate of 2.61×10^{-13} m/cycle. The computed stress intensity factor ranges ΔK are between 0.2 and 1.0 kgf/mm^2, and all of the values are below ΔK_{th}. Therefore, the simulated crack is in Stage I, which is corresponding to the below-threshold region within the FGA. As the crack propagates, ΔK approaches ΔK_{th}, and $\text{d}a/\text{d}N$ gradually increases. Fig. 19(b) shows that the computational results have a good agreement with the experimental investigation. The proposed framework enables the prediction of VHCF crack initiation and propagation processes considering the microstructure of material. The framework provides a new tool for VHCF crack growth analysis and an effective theoretical approach for the introduction of physical mechanism-related internal variables.

5. Conclusions

In the study, a framework based on the coupled CPFEM-CZM constitutive model and the acceleration strategy was proposed to simulate the crack initiation and propagation behavior. The internal variables were transferred between cohesive elements and solid elements. The damage evolution was suggested to be divided into static damage, fatigue initiation damage (Stage I), and fatigue propagation damage (Stage II). The fatigue initiation damage was assumed to be related to the accumulated strain corresponding to the crystal plasticity. Evolution equations of fatigue initiation damage and propagation damage were proposed based on the experimental results. The framework can simulate the crack initiation and propagation under VHCF loading. In the framework, the proportion of crack initiation in the total damage is controlled by adjusting the parameters in the crack initiation damage evolution equation. The proposed acceleration algorithm provides a good equivalence of load cycles and accelerate the model calculation with a certain accuracy.

Sub-cracks sprouting from the internal defects under VHCF were investigated experimentally. The sub-cracks were still in the early stage of fatigue cracking. The framework was used to simulate the sub-crack initiation and propagation process from the internal defect. The calculated results are in good agreement with the experimental results.

It should be noted that the framework is considered as a first step effort, as the model includes significant simplifications and idealizations, including the assumption of crack initiation with accumulated plastic strain, neglecting of dislocation hindrance by

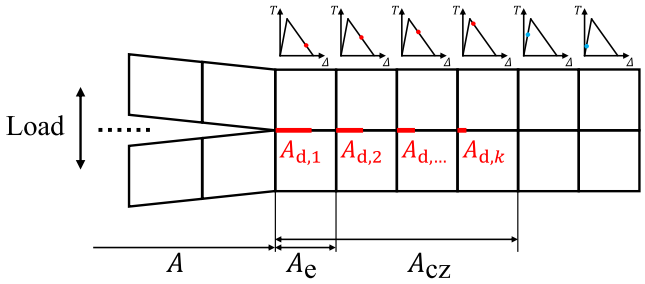

Fig. A.1. Schematic of the cohesive elements at the crack tip.

the grain boundary, and linear suggestion of acceleration strategy. Future work should include expansion of the framework to 3D, account for the dislocation hindrance by the grain boundary, and more in-situ experimental validation, leading to more detailed relations between crack initiation and grain dislocation density.

CRediT authorship contribution statement

Jingyu Sun: Conceptualization, Data curation, Formal analysis, Investigation, Methodology, Software, Validation, Visualization, Writing. **Guian Qian:** Funding acquisition, Supervision. **Jianghua Li:** Investigation. **Ruiyang Li:** Investigation, Validation. **Zhimo Jian:** Validation. **Youshi Hong:** Supervision. **Filippo Berto:** Validation.

Declaration of competing interest

The authors declare that they have no known competing financial interests or personal relationships that could have appeared to influence the work reported in this paper.

Data availability

Data will be made available on request.

Acknowledgments

The present work is financed by the National Natural Science Foundation of China under the contract numbers 12002185, 12272377, 12072345 and 11932020.

Appendix A. Fatigue propagation damage of CZM

The damage of fatigue propagation is based on a fracture mechanics crack growth rate characterization which is achieved by combining fracture mechanics with damage mechanics as follows:

$$\frac{\partial d_{\text{prop}}}{\partial N} = \frac{\partial d_{\text{prop}}}{\partial A_{\text{d}}} \frac{\partial A_{\text{d}}}{\partial N}, \tag{A.1}$$

where A_{d} is the damaged area and $\frac{\partial A_{\text{d}}}{\partial N}$ is the growth rate of the damaged area. The term $\frac{\partial A_{\text{d}}}{\partial N}$ is dependent on the fracture properties of the material and it can be determined experimentally. The term $\frac{\partial d_{\text{prop}}}{\partial A_{\text{d}}}$ can be obtained from the bilinear constitutive law:

$$\frac{\partial d_{\text{prop}}}{\partial A_{\text{d}}} = \frac{1}{A_{\text{e}}} \frac{\left[\bar{\theta}^{\text{f}}(1-d) + d\bar{\theta}^{0}\right]^2}{\bar{\theta}^{\text{f}}\bar{\theta}^{0}}, \tag{A.2}$$

where A_{e} is the element area. As schematically represented in Fig. A.1, it can be assumed that the increase of the crack area A is equivalent to the increase of the amount of damaged area A_{d}. The increase in the damaged area along a crack front is equal to the increase in the damaged area of all of the elements ahead of the crack tip. Therefore, the crack growth rate can be assumed to be equal to the sum of the damaged area growth rates of all damaged elements ahead of the crack tip, that is, all elements in the cohesive zone:

$$\frac{\partial A}{\partial N} = \sum_{k \in A_{\text{CZ}}} \frac{\partial A_{\text{d},k}}{\partial N} = \frac{A_{\text{CZ}}}{A_{\text{e}}} \frac{\partial A_{\text{d}}}{\partial N}, \tag{A.3}$$

where A_{CZ} is the area of the cohesive zone and assuming that the mean area of the elements in the cohesive zone is A_e. The ratio A_{CZ}/A_e represents the number of elements in which the cohesive zone has been divided. Rearranging terms in Eq. (A.3), the surface damage growth rate can be written as

$$\frac{\partial A_d}{\partial N} = \frac{A^e}{A_{CZ}} \frac{\partial A}{\partial N}. \tag{A.4}$$

By introducing Eqs. (A.2) and (A.4) into Eq. (A.1) the evolution of the damage variable as a function of the number of cycles can be written as

$$\frac{\partial d_{prop}}{\partial N} = \frac{1}{A_{CZ}} \frac{\left(\bar{\theta}^f(1-d) + d\bar{\theta}^0\right)^2}{\bar{\theta}^f\bar{\theta}^0} \frac{\partial A}{\partial N}. \tag{A.5}$$

In the study, the crack propagation in region II was defined by the simplest form of Paris Law:

$$\frac{\partial A}{\partial N} = C\left(\frac{\Delta G}{G_c}\right)^m H\left[\left(G - G_{th}\right)\left(G_c - G\right)\right]. \tag{A.6}$$

where A is the crack area, N is the number of cycles. It should be noting that the expression is in a non-standard Paris form. The local quantity ΔG is used as the driven force of the damage of a local element.

Appendix B. Mixed-mode criteria of CZM

The criteria used to predict crack propagation under mixed-mode loading conditions are usually established in terms of the components of the energy release rate and fracture toughness. It is assumed that the crack grows when the energy release rate G exceeds the critical energy release rate G_c. The expression proposed by Benzeggagh and Kenane (1996) for the critical energy release rate G_c of mixed-mode is given as

$$G_c = G_{Ic} + \left(G_{IIc} - G_{Ic}\right)\left(\frac{G_{sh}}{G_{sh} + G_I}\right)^\eta, \tag{B.1}$$

where $G_{sh} = G_{II} + G_{III}$ is the energy release rate for shear loading, and η is a semi-empirical coefficient and η is set as 1 in the present work. Therefore, the interfacial strength T^0 of mixed-mode can be calculated with:

$$\left(T^0\right)^2 = \left(T_1^0\right)^2 + \left[\left(T_2^0\right)^2 - \left(T_1^0\right)^2\right]\left(\frac{G_{sh}}{G_{sh} + G_I}\right)^\eta. \tag{B.2}$$

Appendix C. Stress update algorithm and consistent material Jacobian of CPFEM

To increase the stability of the numerical calculation at a large time step, Peirce et al. (1984) used the tangent coefficient method to improve the calculation of Eq. (7). The shear strain increment in time step Δt is defined as $\Delta\gamma^{(\alpha)}$, then

$$\Delta\gamma^{(\alpha)} = \Delta t\left[(1-\eta)\dot{\gamma}^{(\alpha)}(t) + \eta\dot{\gamma}^{(\alpha)}(t+\Delta t)\right]. \tag{C.1}$$

The parameter η ranges from 0 to 1, with $\eta = 0$ corresponding to the simple Euler time integration scheme. In the present work, η is set as 0.5. The Taylor expansion is used to approximate the last term in Eq. (C.1) as,

$$\dot{\gamma}^{(\alpha)}(t+\Delta t) = \dot{\gamma}^{(\alpha)}(t) + \left.\frac{\partial\dot{\gamma}^{(\alpha)}}{\partial\tau^{(\alpha)}}\right|_t \Delta\tau^{(\alpha)} + \left.\frac{\partial\dot{\gamma}^{(\alpha)}}{\partial\alpha^{(\alpha)}}\right|_t \Delta\alpha^{(\alpha)} + \left.\frac{\partial\dot{\gamma}^{(\alpha)}}{\partial r^{(\alpha)}}\right|_t \Delta r^{(\alpha)}, \tag{C.2}$$

where,

$$\Delta\tau^{(\alpha)} = \dot{\tau}^{(\alpha)}\Delta t, \tag{C.3}$$

$$\Delta\alpha^{(\alpha)} = c_1\Delta\gamma^{(\alpha)} - c_2\left|\Delta\gamma^{(\alpha)}\right|\alpha^{(\alpha)}, \tag{C.4}$$

$$\Delta r^{(\alpha)} = bQ\sum_\beta h_{\alpha\beta}\left(1 - b\rho^{(\beta)}\right)\left|\Delta\gamma^{(\beta)}\right|. \tag{C.5}$$

The shear stress rate at α-th slip system can be expressed by

$$\dot{\tau}^{(\alpha)} = B_{ij}^{(\alpha)} D_{ij} - B_{ij}^{(\alpha)} D_{ij}^p, \tag{C.6}$$

with

$$B_{ij}^{(\alpha)} = \mathbb{C}_{ijkl} P_{kl}^{(\alpha)} + \Omega_{ik}^{(\alpha)}\sigma_{kj}. \tag{C.7}$$

Substituting Eq. (C.2) into Eq. (C.1), we can obtain

$$\Delta\gamma^{(\alpha)} = \Delta t\left[\dot{\gamma}^{(\alpha)}(t) + \eta\left.\frac{\partial\dot{\gamma}^{(\alpha)}}{\partial\tau^{(\alpha)}}\right|_t \Delta\tau^{(\alpha)} + \eta\left.\frac{\partial\dot{\gamma}^{(\alpha)}}{\partial\alpha^{(\alpha)}}\right|_t \Delta\alpha^{(\alpha)} + \eta\left.\frac{\partial\dot{\gamma}^{(\alpha)}}{\partial r^{(\alpha)}}\right|_t \Delta r^{(\alpha)}\right]. \tag{C.8}$$

For convenience, we define

$$X = \frac{\left|\tau^{(\alpha)} - \alpha^{(\alpha)}\right| - r^{(\alpha)}}{\kappa}, \tag{C.9}$$

and a function

$$f^{(\alpha)} = \text{sign}\left(\tau^{(\alpha)} - \alpha^{(\alpha)}\right)\langle X\rangle^n. \tag{C.10}$$

According to the chain rule

$$\frac{\partial\dot{\gamma}^{(\alpha)}}{\partial\tau^{(\alpha)}} = \dot{\gamma}_0\frac{\partial f^{(\alpha)}}{\partial\langle X\rangle}\frac{\partial\langle X\rangle}{\partial\tau^{(\alpha)}} = \dot{\gamma}_0 n\langle X\rangle^{n-1}\frac{1}{\kappa}H(X), \tag{C.11}$$

$$\frac{\partial\dot{\gamma}^{(\alpha)}}{\partial\alpha^{(\alpha)}} = \dot{\gamma}_0\frac{\partial f^{(\alpha)}}{\partial\langle X\rangle}\frac{\partial\langle X\rangle}{\partial\alpha^{(\alpha)}} = -\dot{\gamma}_0 n\langle X\rangle^{n-1}\frac{1}{\kappa}H(X), \tag{C.12}$$

$$\frac{\partial\dot{\gamma}^{(\alpha)}}{\partial r^{(\alpha)}} = \dot{\gamma}_0\frac{\partial f^{(\alpha)}}{\partial\langle X\rangle}\frac{\partial\langle X\rangle}{\partial r^{(\alpha)}} = -\dot{\gamma}_0 n\langle X\rangle^{n-1}\frac{1}{\kappa}H(X)\,\text{sign}\left(\tau^{(\alpha)} - \alpha^{(\alpha)}\right). \tag{C.13}$$

Substituting Eqs. (C.11), (C.12), (C.13) into Eq. (C.8), we can obtain

$$\Delta\gamma^{(\alpha)} = \Delta t\dot{\gamma}^{(\alpha)}(t) + \theta\dot{\gamma}_0 n\langle X\rangle^{n-1}\frac{1}{\kappa}H(X)\left[\Delta\tau^{(\alpha)} - \Delta\alpha^{(\alpha)} - \text{sign}\left(\tau^{(\alpha)} - \alpha^{(\alpha)}\right)\Delta r^{(\alpha)}\right]. \tag{C.14}$$

Substituting Eqs. (C.3), (C.4), (C.5), (C.6) into Eq. (C.14), and noting that $\langle X\rangle^{n-1}H(X) = \langle X\rangle^{n-1}$, we can obtain

$$\begin{aligned}\sum_{\beta=1}^{M}\Big\{&\delta_{\alpha\beta} + \Delta t\eta\dot{\gamma}_0 n\langle X\rangle^{n-1}\frac{1}{\kappa}\left[B_{ij}^{(\alpha)}P_{ij}^{(\beta)} + \delta_{\alpha\beta}\left(c_1 - c_2\text{sign}\left(\dot{\gamma}^{(\beta)}\right)\alpha^{(\alpha)}\right)\right.\\ &\left.+\text{sign}\left(\tau^{(\alpha)} - \alpha^{(\alpha)}\right)bQh_{\alpha\beta}\left(1 - b\rho^{(\beta)}\right)\text{sign}\left(\dot{\gamma}^{(\beta)}\right)\right]\Big\}\Delta\gamma^{(\beta)} = \Delta t\dot{\gamma}^{(\alpha)}(t) + \Delta t\eta\dot{a}^{(\alpha)}n\langle X\rangle^{n-1}\frac{1}{\kappa}B_{ij}^{(\alpha)}\Delta\varepsilon_{ij}.\end{aligned} \tag{C.15}$$

The shear strain increment at each slip system $\Delta\gamma^{(\beta)}$ can be solved from Eq. (C.15).

References

Asgharzadeh, A., Nazari Tiji, S.A., Park, T., Pourboghrat, F., 2022. Prediction of softening kinetics and recrystallization texture in non-isothermally annealed bulged tubes using CPFEM and CA models. Mater. Sci. Eng. A 832, 142308. http://dx.doi.org/10.1016/j.msea.2021.142308.

Bach, J., Möller, J.J., Göken, M., Bitzek, E., Höppel, H.W., 2016. On the transition from plastic deformation to crack initiation in the high- and very high-cycle fatigue regimes in plain carbon steels. Int. J. Fatigue 93, 281–291. http://dx.doi.org/10.1016/j.ijfatigue.2016.04.003.

Barenblatt, G.I., 1962. The mathematical theory of equilibrium cracks in brittle fracture. In: Dryden, H.L., von Kármán, T., Kuerti, G., van den Dungen, F.H., Howarth, L. (Eds.), In: Advances in Applied Mechanics, vol. 7, Elsevier, pp. 55–129. http://dx.doi.org/10.1016/S0065-2156(08)70121-2.

Bellini, C., Berto, F., Cocco, V.D., Iacoviello, F., Mocanu, L.P., Razavi, J., 2021. Additive manufacturing processes for metals and effects of defects on mechanical strength: A review. Procedia Struct. Integr. 33, 498–508. http://dx.doi.org/10.1016/j.prostr.2021.10.057.

Benzeggagh, M., Kenane, M., 1996. Measurement of mixed-mode delamination fracture toughness of unidirectional glass/epoxy composites with mixed-mode bending apparatus. Compos. Sci. Technol. 56 (4), 439–449. http://dx.doi.org/10.1016/0266-3538(96)00005-X.

Bergsmo, A., Dunne, F.P.E., 2020. Competing mechanisms of particle fracture, decohesion and slip-driven fatigue crack nucleation in a PM nickel superalloy. Int. J. Fatigue 135, 105573. http://dx.doi.org/10.1016/j.ijfatigue.2020.105573.

Briffod, F., Shiraiwa, T., Enoki, M., 2018. Numerical investigation of the influence of rolling texture and microstructure on fatigue crack initiation in BCC polycrystals. Int. J. Fatigue 107, 72–82. http://dx.doi.org/10.1016/j.ijfatigue.2017.10.019.

Cheng, J., Lane, R., Kesler, M.S., Brechtl, J., Hu, X., Mirzaeifar, R., Rios, O., Momen, A.M., Nawaz, K., 2021. Experiment and non-local crystal plasticity finite element study of nanoindentation on Al-8Ce-10Mg alloy. Int. J. Solids Struct. 233, 111233. http://dx.doi.org/10.1016/j.ijsolstr.2021.111233.

Cong, T., Li, R., Zheng, Z., Ma, X., Wu, S., Zhang, R., Berto, F., Sun, J., Qian, G., 2022. Experimental and computational investigation of weathering steel Q450NQR1 under high cycle fatigue loading via crystal plasticity finite element method. Int. J. Fatigue 159, 106772. http://dx.doi.org/10.1016/j.ijfatigue.2022.106772.

Dugdale, D.S., 1960. Yielding of steel sheets containing slits. J. Mech. Phys. Solids 8 (2), 100–104. http://dx.doi.org/10.1016/0022-5096(60)90013-2.

Ghisi, N.B., Ramos, H., Kindleyside, L., Aboulkhair, N.T., Santiago, R., 2022. The influence of the characteristic microstructure of additively manufactured AlSi10Mg on the plastic behaviour at various strain rates. Mater. Des. 223, 111112. http://dx.doi.org/10.1016/j.matdes.2022.111112.

Ghodrati, M., Ahmadian, M., Mirzaeifar, R., 2019. Three-dimensional study of rolling contact fatigue using crystal plasticity and cohesive zone method. Int. J. Fatigue 128, http://dx.doi.org/10.1016/j.ijfatigue.2019.105208.

Gu, C., Lian, J., Lv, Z., Bao, Y., 2022. Microstructure-based fatigue modeling with residual stresses: Effect of inclusion shape on very high cycle fatigue life. Crystals 12 (2), 200. http://dx.doi.org/10.3390/cryst12020200.

Hong, Y., Lei, Z., Sun, C., Zhao, A., 2014. Propensities of crack interior initiation and early growth for very-high-cycle fatigue of high strength steels. Fatigue Crack Paths 2012, Int. J. Fatigue Fatigue Crack Paths 2012, 58, 144–151.http://dx.doi.org/10.1016/j.ijfatigue.2013.02.023,

Hong, Y., Liu, X., Lei, Z., Sun, C., 2016. The formation mechanism of characteristic region at crack initiation for very-high-cycle fatigue of high-strength steels. Int. J. Fatigue 89, 108–118. http://dx.doi.org/10.1016/j.ijfatigue.2015.11.029.

Hu, J., Zhuang, Z., Liu, F., Liu, X., Liu, Z., 2019. Investigation of grain boundary and orientation effects in polycrystalline metals by a dislocation-based crystal plasticity model. Comput. Mater. Sci. 159, 86–94. http://dx.doi.org/10.1016/j.commatsci.2018.12.010.

Huang, X., Wang, J., Zhao, S., Yao, Z., Liu, C., 2021. High-resolution multiscale modeling of mechanical behavior of cold-drawn pearlitic steels. J. Mater. Res. Technol. 15, 5920–5935. http://dx.doi.org/10.1016/j.jmrt.2021.10.087.

Indeck, J., Demeneghi, G., Mayeur, J., Williams, C., Hazeli, K., 2021. Influence of reversible and non-reversible fatigue on the microstructure and mechanical property evolution of 7075-T6 aluminum alloy. Int. J. Fatigue 145, 106094. http://dx.doi.org/10.1016/j.ijfatigue.2020.106094.

Jian, Z.M., Qian, G.A., Paolino, D.S., Tridello, A., Berto, F., Hong, Y.S., 2021. Crack initiation behavior and fatigue performance up to very-high-cycle regime of AlSi10Mg fabricated by selective laser melting with two powder sizes. Int. J. Fatigue 143, 106013. http://dx.doi.org/10.1016/j.ijfatigue.2020.106013.

Karamitros, V., MacLachlan, D.W., Dunne, F.P., 2022. Mechanistic fatigue in Ni-based superalloy single crystals: A study of crack paths and growth rates. J. Mech. Phys. Solids 158, 104663. http://dx.doi.org/10.1016/j.jmps.2021.104663.

Li, P., Jiang, W., Rui, S.-S., Yao, W.-x., Shi, H.-j., Han, Q.-n., Huang, J., 2021. Effect of misorientation on the fatigue life of nickel-base single crystal superalloy DD5 at 980 °C. Int. J. Fatigue 153, 106479. http://dx.doi.org/10.1016/j.ijfatigue.2021.106479.

Li, J., Sun, J., Li, Y., Qian, G., Wang, Z., 2022a. Very-high-cycle fatigue induced growth and amorphization of Si particles in additively manufactured AlSi10Mg alloy: Dependence of applied stress ratio. Int. J. Fatigue 164, 107167. http://dx.doi.org/10.1016/j.ijfatigue.2022.107167.

Li, J., Sun, J., Qian, G., Shi, L., 2022b. Defect-induced cracking and fine granular characteristics in very-high-cycle fatigue of laser powder bed fusion AlSi10Mg alloy. Int. J. Fatigue 158, 106770. http://dx.doi.org/10.1016/j.ijfatigue.2022.106770.

Li, H., Sun, X., Yang, H., 2016. A three-dimensional cellular automata-crystal plasticity finite element model for predicting the multiscale interaction among heterogeneous deformation, DRX microstructural evolution and mechanical responses in titanium alloys. Int. J. Plast. 87, 154–180. http://dx.doi.org/10.1016/j.ijplas.2016.09.008.

Li, X.P., Wang, X.J., Saunders, M., Suvorova, A., Zhang, L.C., Liu, Y.J., Fang, M.H., Huang, Z.H., Sercombe, T.B., 2015a. A selective laser melting and solution heat treatment refined Al–12Si alloy with a controllable ultrafine eutectic microstructure and 25% tensile ductility. Acta Mater. 95, 74–82. http://dx.doi.org/10.1016/j.actamat.2015.05.017.

Li, H., Yuan, H., Li, X., 2015b. Assessment of low cycle fatigue crack growth under mixed-mode loading conditions by using a cohesive zone model. Int. J. Fatigue 75, 39–50. http://dx.doi.org/10.1016/j.ijfatigue.2015.01.008.

Liang, Y.-J., Dávila, C.G., Iarve, E.V., 2021. A reduced-input cohesive zone model with regularized extended finite element method for fatigue analysis of laminated composites in Abaqus. Compos. Struct. 275, 114494. http://dx.doi.org/10.1016/j.compstruct.2021.114494.

Liu, L.Y., Yang, Q.S., Liu, X., Shang, J.J., 2021a. Modeling damage evolution of Graphene/Aluminum composites considering crystal cracking and interface failure. Compos. Struct. 267, 113863. http://dx.doi.org/10.1016/j.compstruct.2021.113863.

Liu, G., Zhang, X., Chen, X., He, Y., Cheng, L., Huo, M., Yin, J., Hao, F., Chen, S., Wang, P., Yi, S., Wan, L., Mao, Z., Chen, Z., Wang, X., Cao, Z., Lu, J., 2021b. Additive manufacturing of structural materials. Mater. Sci. Eng. R 145, 100596. http://dx.doi.org/10.1016/j.mser.2020.100596.

Min, K.M., Jeong, W., Hong, S.H., Lee, C.A., Cha, P.R., Han, H.N., Lee, M.G., 2020. Integrated crystal plasticity and phase field model for prediction of recrystallization texture and anisotropic mechanical properties of cold-rolled ultra-low carbon steels. Int. J. Plast. 127, 102644. http://dx.doi.org/10.1016/j.ijplas.2019.102644.

Molter, D.L., de Castro, M.A.L., Silva dos Santos, D., 2021. Role of hydrogen in the separation of interfaces in S13Cr supermartensitic stainless steel. Acta Mater. 206, 116614. http://dx.doi.org/10.1016/j.actamat.2020.116614.

Morgeneyer, T.F., Khadyko, M., Buljac, A., Helfen, L., Hild, F., Benallal, A., Bø rvik, T., Hopperstad, O.S., 2021. On crystallographic aspects of heterogeneous plastic flow during ductile tearing: 3D measurements and crystal plasticity simulations for AA7075-T651. Int. J. Plast. 144, 103028. http://dx.doi.org/10.1016/j.ijplas.2021.103028.

Mughrabi, H., 2009. Cyclic slip irreversibilities and the evolution of fatigue damage. Metall. Mater. Trans. B 40 (4), 431–453. http://dx.doi.org/10.1007/s11663-009-9240-4.

Murakami, Y., 2019. 5 - effect of hardness HV on fatigue limits of materials containing defects, and fatigue limit prediction equations. In: Murakami, Y. (Ed.), Metal Fatigue (Second Edition), second ed. Academic Press, pp. 61–94. http://dx.doi.org/10.1016/B978-0-12-813876-2.00005-4.

Nguyen, N.H.T., Bui, H.H., Kodikara, J., Arooran, S., Darve, F., 2019. A discrete element modelling approach for fatigue damage growth in cemented materials. Int. J. Plast. 112, 68–88. http://dx.doi.org/10.1016/j.ijplas.2018.08.007.

Ogawa, T., Stanzl-Tschegg, S.E., Schönbauer, B.M., 2014. A fracture mechanics approach to interior fatigue crack growth in the very high cycle regime. Eng. Fract. Mech. 115, 241–254. http://dx.doi.org/10.1016/j.engfracmech.2013.11.007.

Paepegem, W.V., Degrieck, J., Baets, P.D., 2001. Finite element approach for modelling fatigue damage in®bre-Reinforced composite materials. Part B 14.

Pan, X., Hong, Y., 2019. High-cycle and very-high-cycle fatigue behaviour of a titanium alloy with equiaxed microstructure under different mean stresses. Fatigue Fract. Eng. Mater. Struct. 42 (9), 1950–1964. http://dx.doi.org/10.1111/ffe.13050.

Pan, X., Qian, G., Hong, Y., 2021. Nanograin formation in dimple ridges due to local severe-plastic-deformation during ductile fracture. Scr. Mater. 194, 113631. http://dx.doi.org/10.1016/j.scriptamat.2020.113631.

Paul, M.J., Liu, Q., Best, J.P., Li, X., Kruzic, J.J., Ramamurty, U., Gludovatz, B., 2021. Fracture resistance of AlSi10Mg fabricated by laser powder bed fusion. Acta Mater. 211, 116869. http://dx.doi.org/10.1016/j.actamat.2021.116869.

Peirce, D., Asaro, R.J., Needleman, A., 1982. An analysis of nonuniform and localized deformation in ductile single crystals. Acta Metall. 30 (6), 1087–1119. http://dx.doi.org/10.1016/0001-6160(82)90005-0.

Peirce, D., Shih, C., Needleman, A., 1984. A tangent modulus method for rate dependent solids. Comput. Struct. 18 (5), 875–887. http://dx.doi.org/10.1016/0045-7949(84)90033-6.

Qian, G., Jian, Z., Qian, Y., Pan, X., Ma, X., Hong, Y., 2020. Very-high-cycle fatigue behavior of AlSi10Mg manufactured by selective laser melting: Effect of build orientation and mean stress. Int. J. Fatigue 138, 105696. http://dx.doi.org/10.1016/j.ijfatigue.2020.105696.

Qian, W., Wu, S., Wu, Z., Ahmed, S., Zhang, W., Qian, G., Withers, P.J., 2022. In situ X-ray imaging of fatigue crack growth from multiple defects in additively manufactured AlSi10Mg alloy. Int. J. Fatigue 155, 106616. http://dx.doi.org/10.1016/j.ijfatigue.2021.106616.

Ritz, F., Staecker, C., Beck, T., Sander, M., 2018. FGA formation mechanism for X10CrNiMoV12-2-2 and 34CrNiMo6 for constant and variable amplitude tests under the influence of applied mean loads. Fatigue Fract. Eng. Mater. Struct. 41 (7), 1576–1587. http://dx.doi.org/10.1111/ffe.12797.

Roe, K.L., Siegmund, T., 2003. An irreversible cohesive zone model for interface fatigue crack growth simulation. Eng. Fract. Mech. 70 (2), 209–232. http://dx.doi.org/10.1016/S0013-7944(02)00034-6.

Roters, F., Eisenlohr, P., Hantcherli, L., Tjahjanto, D.D., Bieler, T.R., Raabe, D., 2010. Overview of constitutive laws, kinematics, homogenization and multiscale methods in crystal plasticity finite-element modeling: Theory, experiments, applications. Acta Mater. 58 (4), 1152–1211. http://dx.doi.org/10.1016/j.actamat.2009.10.058.

Roy, U., McDowell, D.L., Zhou, M., 2021. Effect of grain orientations on fracture behavior of polycrystalline metals. J. Mech. Phys. Solids 151, 104384. http://dx.doi.org/10.1016/j.jmps.2021.104384.

Roy, U., Zhou, M., 2020. A computational framework for predicting the fracture toughness of metals as function of microstructure. J. Mech. Phys. Solids 142, 103955. http://dx.doi.org/10.1016/j.jmps.2020.103955.

Sakai, T., Oguma, N., Morikawa, A., 2015. Microscopic and nanoscopic observations of metallurgical structures around inclusions at interior crack initiation site for a bearing steel in very high-cycle fatigue. Fatigue Fract. Eng. Mater. Struct. 38 (11), 1305–1314. http://dx.doi.org/10.1111/ffe.12344.

Sander, M., Müller, T., Lebahn, J., 2014. Influence of mean stress and variable amplitude loading on the fatigue behaviour of a high-strength steel in VHCF regime. Int. J. Fatigue 62, 10–20. http://dx.doi.org/10.1016/j.ijfatigue.2013.04.015.

Shang, X., Zhang, H., Wang, L., Zhu, G., Cui, Z., Fu, M.W., Zeng, X., 2021. The effect of stress state and strain partition mode on the damage behavior of a Mg-Ca alloy. Int. J. Plast. 144, 103040. http://dx.doi.org/10.1016/j.ijplas.2021.103040.

Shen, F., Münstermann, S., Lian, J., 2022. A unified fracture criterion considering stress state dependent transition of failure mechanisms in bcc steels at –196 °C. Int. J. Plast. 156, 103365. http://dx.doi.org/10.1016/j.ijplas.2022.103365.

Shiozawa, K., Morii, Y., Nishino, S., Lu, L., 2006. Subsurface crack initiation and propagation mechanism in high-strength steel in a very high cycle fatigue regime. Int. J. Fatigue 28 (11), 1521–1532. http://dx.doi.org/10.1016/j.ijfatigue.2005.08.015.

Strubbia, R., Hereñú, S., Giertler, A., Alvarez-Armas, I., Krupp, U., 2014. Experimental characterization of short crack nucleation and growth during cycling in lean duplex stainless steels. Int. J. Fatigue 65, 58–63. http://dx.doi.org/10.1016/j.ijfatigue.2013.08.023.

Su, H., Liu, X., Sun, C., Hong, Y., 2017. Nanograin layer formation at Crack Initiation Region for very-high-cycle fatigue of a Ti-6Al-4V alloy. Fatigue Fract. Eng. Mater. Struct. 40 (6), 979–993. http://dx.doi.org/10.1111/ffe.12562.

Sun, C., Wu, H., Chi, W., Wang, W., Zhang, G.-P., 2022. Nanograin formation and cracking mechanism in Ti alloys under very high cycle fatigue loading. Int. J. Fatigue 107331. http://dx.doi.org/10.1016/j.ijfatigue.2022.107331.

Turon, A., Camanho, P.P., Costa, J., Renart, J., 2010. Accurate simulation of delamination growth under mixed-mode loading using cohesive elements: Definition of interlaminar strengths and elastic stiffness. Compos. Struct. 92 (8), 1857–1864. http://dx.doi.org/10.1016/j.compstruct.2010.01.012.

Turon, A., Costa, J., Camanho, P., Dávila, C., 2007. Simulation of delamination in composites under high-cycle fatigue. Composites A 38 (11), 2270–2282. http://dx.doi.org/10.1016/j.compositesa.2006.11.009.

Wang, Q., Berard, J., Rathery, S., Bathias, C., 1999. High-cycle fatigue crack initiation and propagation behaviour of high-strength spring steel wires. Fatigue Fract. Eng. Mater. Struct. 22 (8), 673–677. http://dx.doi.org/10.1046/j.1460-2695.1999.00184.x.

Ye, L., 1988. Role of matrix resin in delamination onset and growth in composite laminates. Compos. Sci. Technol. 33 (4), 257–277. http://dx.doi.org/10.1016/0266-3538(88)90043-7.

Yuan, H., Li, X., 2018. Critical remarks to cohesive zone modeling for three-dimensional elastoplastic fatigue crack propagation. Eng. Fract. Mech. 202, 311–331. http://dx.doi.org/10.1016/j.engfracmech.2018.03.018.

Zhang, J., Li, J., Wu, S., Zhang, W., Sun, J., Qian, G., 2022. High-cycle and very-high-cycle fatigue lifetime prediction of additively manufactured AlSi10Mg via crystal plasticity finite element method. Int. J. Fatigue 155, 106577. http://dx.doi.org/10.1016/j.ijfatigue.2021.106577.

Zhang, H.J., Yu, F., Li, S.X., He, E.G., 2021. Fine Granular Area formation by damage-induced shear strain localization in very-high-cycle fatigue. Fatigue Fract. Eng. Mater. Struct. 44 (9), 2489–2502. http://dx.doi.org/10.1111/ffe.13529.

Zhao, Q., Abdel Wahab, M., Ling, Y., Liu, Z., 2021. Fatigue crack propagation within Al-Cu-Mg single crystals based on crystal plasticity and XFEM combined with cohesive zone model. Mater. Des. 210, 110015. http://dx.doi.org/10.1016/j.matdes.2021.110015.

Zhu, M.L., Jin, L., Xuan, F.Z., 2018. Fatigue life and mechanistic modeling of interior micro-defect induced cracking in high cycle and very high cycle regimes. Acta Mater. 157, 259–275. http://dx.doi.org/10.1016/j.actamat.2018.07.036.